Circuits and Systems
Mekelweg 4,
2628 CD Delft
The Netherlands
https://sps.ewi.tudelft.nl/

SPS-2023-00

M.Sc. Thesis

Coherent integration for imaging and detection using active sonar

Kaan Demir B.Sc.

Abstract

Existing sonar systems typically rely on a minimum signal strength of a single echo, which limits their performance in low signal-to-noise conditions. This thesis explores the concept of coherent integration for active sonar, with the aim of improving imaging and detection capabilities under low signal-to-noise conditions. The goal is to provide signal processing methods that achieve long-time coherent integration of the received echoes, thereby maximising the processing gain. Additionally, this research explores waveform design by comparing the performance of pseudo-random noise with chirps. Two applications are seen in this thesis: moving target detection, which involves static sonar sensors, and synthetic aperture imaging, where the sensors move while the imaging scene remains static. For moving target detection, a processing methods is proposed which achieves coherent integration for constant velocity targets in a computationally efficient manner, and improves the detection performance by implementing a clutter filtering stage. For the second application, a processing method for imaging from a moving sensor pair is proposed. The resulting point-spread function for a circular sensor trajectory is investigated, from which a set of design rules are established. Additionally, a least squares algorithm is applied, which shows that the resulting image can be improved in terms of resolution and sidelobe interference. Finally, the imaging and detection methods are tested and verified using an in-air demonstrator.

Faculty of Electrical Engineering, Mathematics and Computer Science
Delft University of Technology

Coherent integration for imaging and detection using active sonar

THESIS

submitted in partial fulfillment of the
requirements for the degree of

MASTER OF SCIENCE

in

ELECTRICAL ENGINEERING

by

Kaan Demir B.Sc.
born in Nieuwegein, The Netherlands

This work was performed in:

Circuits and Systems Group
Department of Microelectronics
Faculty of Electrical Engineering, Mathematics and Computer Science
Delft University of Technology

Delft University of Technology

Delft University of Technology
Department of
Microelectronics

The undersigned hereby certify that they have read and recommend to the Faculty of Electrical Engineering, Mathematics and Computer Science for acceptance a thesis entitled **"Coherent integration for imaging and detection using active sonar"** by **Kaan Demir B.Sc.** in partial fulfillment of the requirements for the degree of **Master of Science**.

Dated: June 28, 2023. Public release after embargo: Dec. 28, 2023

Chairman: ______________________
prof.dr.ir. Geert Leus

Advisor: ______________________
prof.dr.ir. Geert Leus

Committee Members: ______________________
dr.ir. Yanki Aslan

____
dr.ir. Vsevolod Kovalenko

Abstract

Existing sonar systems typically rely on a minimum signal strength of a single echo, which limits their performance in low signal-to-noise conditions. This thesis explores the concept of coherent integration for active sonar, with the aim of improving imaging and detection capabilities under low signal-to-noise conditions. The goal is to provide signal processing methods that achieve long-time coherent integration of the received echoes, thereby maximising the processing gain. Additionally, this research explores waveform design by comparing the performance of pseudo-random noise with chirps. Two applications are seen in this thesis: moving target detection, which involves static sonar sensors, and synthetic aperture imaging, where the sensors move while the imaging scene remains static. For moving target detection, a processing methods is proposed which achieves coherent integration for constant velocity targets in a computationally efficient manner, and improves the detection performance by implementing a clutter filtering stage. For the second application, a processing method for imaging from a moving sensor pair is proposed. The resulting point-spread function for a circular sensor trajectory is investigated, from which a set of design rules are established. Additionally, a least squares algorithm is applied, which shows that the resulting image can be improved in terms of resolution and sidelobe interference. Finally, the imaging and detection methods are tested and verified using an in-air demonstrator.

Acknowledgments

This work has been made possible in collaboration with Fugro, and I would like to extend my thanks to Alle-Jan van der Veen for facilitating this connection. Many thanks to Vsevolod Kovalenko and Arnoud Jongsma for your warm-hearted welcome to the company. I am grateful for the opportunity to be a part of this exciting project.

I would like to thank my supervisor Geert Leus for his assistance during this project. I am truly appreciative of the freedom I was given to explore and develop my own ideas, while you were always approachable and available for any questions.

A special thanks to Vsevolod, for providing me with weekly guidance and additional nuggets of wisdom. Finally, thanks to Pim van der Meulen for giving awesome feedback throughout this project. Your support and friendship have certainly made these past months much more manageable and enjoyable.

Kaan Demir
Delft, The Netherlands
June 20, 2023

Contents

List of Figures

Introduction 1

Active sonar refers to the technique of measuring the distance to an underwater object, by means of transmitting a pulse of sound, commonly referred to as a 'ping', and subsequently listening to the echo. By analysing the delay of the received echo, the distance to the object can be determined, using the speed of sound in water ($c \approx 1500$ m/s). This basic mechanism is depicted in Figure 1.1. Sonar systems are typically mounted on the hull of a ship, e.g., to determine the depth of the seabed, or to detect certain objects under the ship, such as a school of fish.

The use of sonar is particularly preferred for underwater surveillance systems. This is primarily because of the low attenuation of sound in water, which surpasses that other surveillance methods such as radar or visual. It can be used to detect moving targets such as human divers, for example, in an intruder alarm system to protect a harbour from underwater terrorist threats. State-of-the-art active sonar systems capable of detecting moving targets most often rely on beamforming to make an 'echograph', which shows the positions of objects that have a strong echo [2]. The detection of a moving target is addressed by looking for tracks that form in the echograph, which is updated after each transmitted pulse. Hence, the response of the moving target signal in the echograph is constrained to the strength of a single echo. The maximum detection range of such systems may vary, but is several hundred of meters at most. This limitation often restricts the coverage of the system to the immediate waters of the harbour. Increasing the detection range potentially enables the detection of an intruder approaching the harbour. This would allow the operator to respond sooner, consequently reducing the risk of harm posed by the intruder. However, detecting long-range or weakly reflecting targets is challenging, due to a low signal-to-noise ratio (SNR) of a single echo, making it difficult to detect. This motivates the need to extend the coherent processing interval to integrate the signal of multiple pulses. In addition,

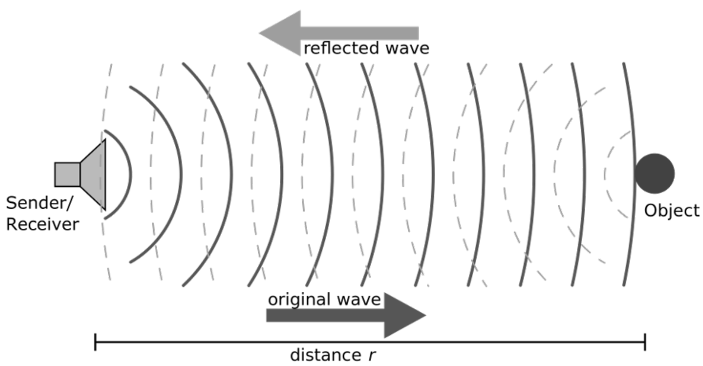

Figure 1.1: Schematic showing the fundamental principle of active sonar, by courtesy of [1].

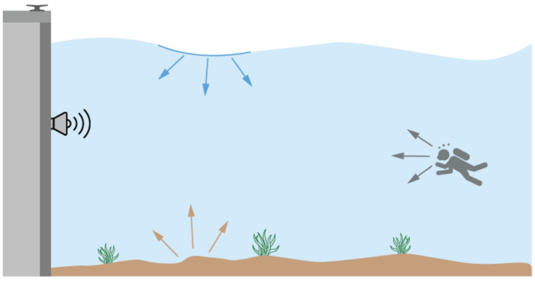

(a) Sonar system for detecting a moving target

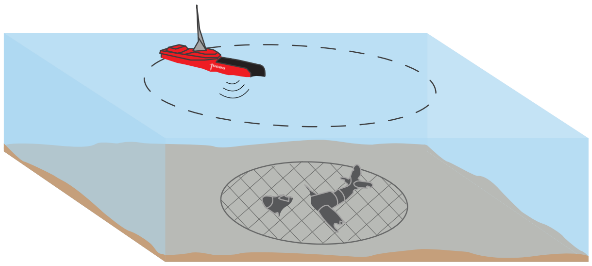

(b) Sonar system for synthetic aperture imaging

Figure 1.2: Schematic drawing of the envisioned sonar systems for imaging and detection.

a disadvantage of existing systems for long-range detection is increased attenuation, due to the high frequencies used for beamforming, with typical carrier frequencies of around 100 kHz [2]. Therefore, the idea of using low-to-medium (10-100 kHz) frequency sonar for lower absorption, combined with coherent integration over multiple pulses, is considered in this thesis for improving long-range detection of moving targets. To illustrate the problem, a schematic for moving target detection is shown in Figure 1.2. As indicated by the arrows, the sonar not only receives echoes from the target but also from the environment, including the seabed and the (moving) sea surface, which introduces additional challenges for detecting the moving target.

Sonar can also be used to make images of the seabed, or static structures that lie on the seabed, such as pipelines or shipwrecks. Imaging sonars typically use an array of sonar elements for directional signal transmission and reception, by using beamforming [3]. An example is the multibeam echosounder, which relies on the technique of beamforming to map the received echoes to a 3D image of the seabed. In such a system, the transmit and receive array are placed in a 'Mills Cross' arrangement, to steer a narrow transmit beam in the across-track direction, and a narrow receive beam in the along-track direction of the ship. Another type of imaging sonar is synthetic aperture sonar (SAS). SAS refers to the technique of coherently combining the echoes of multiple pulses from a moving platform, thereby forming a larger 'synthetic' array [4]. The advantage of a SAS system is that a higher imaging resolution is obtained, than that of the aperture provided by the physical array. However, accurate positioning of the system is required in order to coherently integrate the echoes of multiple pulses. More specifically, the accuracy in positioning required is a small fraction of the wavelength, which can be hard to achieve for high frequency (above 100 kHz) systems [5]. Current implementations of SAS use high frequencies for beamforming, but often rely on micro-navigation, to compensate for the lack of positioning accuracy that is required for these frequencies. Micro-navigation is achieved by exploiting the correlation of the echo signal measured from different sensor positions [6]. This puts a requirement on the minimum SNR that is needed for a single echo, which poses challenges to employ SAS in a low SNR scenario. To overcome these challenges, an interest is taken in low-to-medium frequency systems (in the order of 10 kHz), since fully coherent apertures can be synthesised over long distances using accurate positioning of the sensors. One approach to maximise the exposure and capture the scene from all angles is to follow a circular trajectory (known as circular SAS) [7]. Similarly to long-range moving target detection, the proposed frequency range can be considered for long-range SAS, e.g., for imaging from the surface at increased depths. Another potential application of using low frequencies is that penetration in the seabed is increased, which could be used to image or detect (partially) buried objects on the seabed, such as pipelines or unexploded ordnances (UXO). The processing methods to achieve such large coherent apertures from a moving platform are considered in the second part of this thesis. In Figure 1.2, a possible application of SAS imaging from an unmanned surface vessel is illustrated.

The goal of this thesis is to provide signal processing methods for improving the coherent integration time of a low-to-medium frequency sonar system. This can be considered a missing link in sonar signal processing, and is therefore explored in this thesis, with the aim of imaging and detection under low SNR conditions. In order to maximise the SNR gain, a continuous wave[1] pseudo-random noise (CW PRN) transmit signal is considered for imaging and detection. The performance of pseudo-random noise is compared to more traditional signals, such as chirps. Two applications of long time coherent integration are considered: detection of moving targets (chapter 2), and synthetic aperture imaging (chapter 3). The main difference between the two applications is that for imaging the sensor position relative to the (static) scene is assumed to be accurately known over time, while the motion of a moving target is generally unknown. From this perspective, the integration time for synthetic aperture imaging could be arbitrarily long. However, for moving target detection we need to model the motion, e.g, with a constant velocity, which in practice remains valid for a limited duration.

1.1 Thesis outline

The preliminary work is provided in section 1.2.1, where first the proposed low-to-medium operating frequencies for imaging and detection are substantiated. Secondly, in section 1.2.2 the matched filter for ranging is explained as the basic detection principle of a sonar.

In section 2.1, the matched filter response is extended to Doppler shifted signals (ambiguity function), comparing the correlation properties of PRN and chirps. Next, in section 2.2 a signal model is derived for a constant velocity moving target. Using this model, a method is proposed for imaging a moving target in the presence of clutter interference, which utilises a Radon-Fourier transform to achieve coherent integration over multiple pulses. The method is tested and verified in section 2.3 on synthetic data and using an in-air demonstrator for moving target detection. Here it is shown that HFM outperforms PRN for coherent integration over multiple pulses. Finally, the applicability of the proposed method to a real-world scenario is discussed in section 2.4.

In section 3.1, coherent integration is applied to synthetic aperture imaging. Here,

[1]Continuous wave in some texts refers to a waveform with constant frequency and amplitude. However, here continuous wave refers to a waveform that is continuously on, in contrast to a pulsed signal which includes silences in the transmission.

a signal model is derived for the received echoes using the estimated delays of the signal over the trajectory of the sensors. Using this model, a matched filter for imaging is derived and the point-spread-function (PSF) of the system is analysed. Next, in section 3.2 an attempt is made to improve the imaging resolution by solving the inverse problem, which is tackled using regularised least squares. In section 3.3, the imaging methods are also tested and verified in the in-air demonstrator. The comparison between PRN and HFM is repeated, which shows that PRN has better imaging performance.

Finally, the most important conclusions of this thesis are repeated and some suggestions for future work are discussed in chapter 4.

1.2 Background

To substantiate the use of low-to-medium frequencies for long-range imaging and detection, section 1.2.1 provides a simplified link budget analysis on the SNR as a function of the operating frequency. Thereafter, the idea of pulse compression as the basis of sonar signal processing, is explained in section 1.2.2.

1.2.1 Sonar equation

The sonar equation is used to estimate the performance (in terms of SNR) of a sonar system, dependent on different parameters, such as the operating frequency. Below, the sonar equation is given [8], and some estimates are provided to justify the proposed frequency range for long-range detection:

$$SNR = SL + PG + TS - TPL - NL \tag{1.1}$$

- The source level (SL) is commonly defined in sonar as the ratio of transmit source intensity, I, to a reference intensity, $I_{ref} = 6.67 \cdot 10^{-}19\ W/m^2$. This can alternatively be expressed in terms of the source power P_s in Watts, as: $SL = 10log_{10}(\frac{I}{I_{ref}}) = 10log_{10}(\frac{P_s}{4\pi I_{ref}}) = 10log_{10}(P_s) + 170$ dB.
- The processing gain (PG) depends on the bandwidth B and the duration T over which the target signal is coherently integrated, and is given by $PG = 10log_{10}(BT)$.
- The target strength (TS) is the coefficient describing the ratio of the power that is reflected from a target relative to the incident power. For example, the target strength of a diver, which is assumed to be constant over the considered frequency range, is estimated to be around -20 dB [9].
- The total path loss (TPL) is given by the geometrical spreading of the signal plus the absorption of the signal in water. For spherical spreading the two-way path loss increases with $1/R^4$.

$$TPL_{spherical} = 40log_{10}(R) + 2TL, \tag{1.2}$$

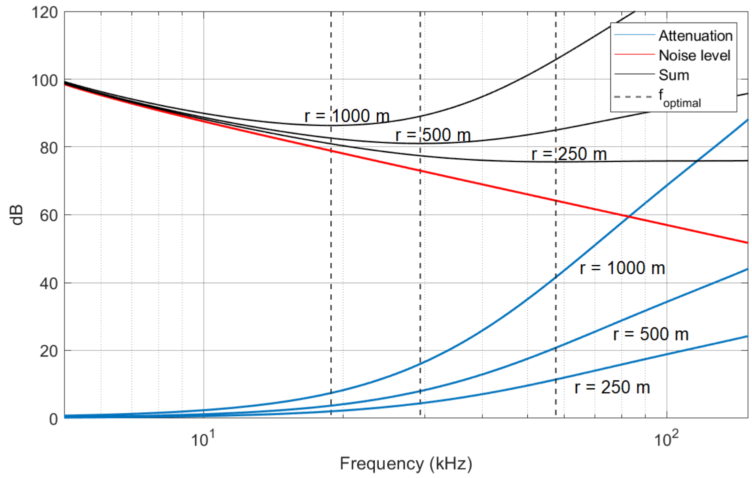

Figure 1.3: The frequency dependent losses in SNR due to noise and attenuation. An optimal frequency is found by minimising the sum of the noise level and the attenuation. For ranges above 250 m attenuation plays a significant role, thereby lowering the optimal operating frequency of the system. The optimal frequencies in this figure are given by 58 kHz at 250 m, 29 kHz at 500 m and 19 kHz at 1000 m range.

where TL is the transmission loss caused by absorption in the water, and given by

$$TL = \frac{\alpha R}{1000}, \quad \alpha = 3.3 \cdot 10^{-3} + \frac{0.11 f^2}{1 + f^2} + \frac{44 f^2}{4100 + f^2} + 3 \cdot 10^{-4} f^2. \tag{1.3}$$

For the noise level NL, an empirical model of the ambient noise level based on harbour measurements is used [9]. According to this model, the noise level in dB relative to $1\mu Pa^2$ (which cancels with the reference intensity of the SL), is given by

$$NL = 170 + 10log_{10}\left(\frac{1}{2(f_c - \frac{B}{2})^2} - \frac{1}{2(f_c + \frac{B}{2})^2}\right). \tag{1.4}$$

In this model, the operating frequency only has an influence on the noise level and the signal attenuation. In short, the lower frequency range contains a higher ambient noise level and higher frequencies suffer more from attenuation. Therefore, an optimal frequency is estimated by minimising the losses due to the combined effect of noise and attenuation as seen in Figure 1.3. A centre frequency of up to 20 kHz could be considered for a range up to 1000 meter, above which the attenuation will cause a significant loss of SNR. However, better estimates of the optimal frequency could be made, using a more accurate model for the noise characteristics specific to the site being observed, e.g., by measuring it.

In the rest of this thesis, two different frequency ranges will be extensively used, one relating to the signals used for the in-air measurements and one relating to the signals used during the harbour trials conducted by Fugro. For the in-air measurements, a tweeter is used as transmitter and a set of analog microphones act as receivers. The signal used during these measurements employ a centre frequency of $f_c = 8$ kHz with a bandwidth of $B = 8$ kHz, giving the frequency range $f \in [4, 12]$ kHz. The signals considered for the initial harbour trials use a centre frequency of $f_c = 12.5$ kHz and a bandwidth of 5 kHz, giving the frequency range $f \in [10, 15]$ kHz. It is important to note that the frequencies are chosen to accommodate the hardware that was available for the measurements, and might not be ideal in terms of the sonar equation. The signals provided in this thesis merely serve as a means to compare different methods or results. They might therefore differ in frequency range from the signals ideally used for imaging and detection purposes.

1.2.2 Pulse compression

Radar and sonar systems require resolution in range in order to estimate the distance to a target. A high range resolution could be achieved by sending very short pulses so that the distance to the target can be computed from the delay of the reflected pulse

$$R = \frac{c\Delta t}{2}, \tag{1.5}$$

using the propagation speed in the medium c (in m/s). A disadvantage of using very short pulses is that the average transmitted power is low and therefore a loud 'ping' is required. Pulse compression is a technique used to obtain good range resolution for longer (modulated) pulses by correlating the received signal with the transmitted pulse. The advantage is that the average transmit power is potentially increased, which increases the SNR at the receiver, thus the maximum detection range of the system [10]. Another point of view is that for the same transmit power, the required peak power is reduced as compared to a short pulse with similar performance.

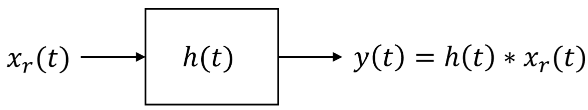

Figure 1.4: Structure of a linear time-invariant filter.

Given the (noise-free) received signal $x_r(t)$, the output of a linear time-invariant filter is given by the convolution with a filter $h(t)$, as seen in Figure 1.4.

$$y(t) = \int_{-\infty}^{\infty} h(t-\tau)x_r(\tau)d\tau. \tag{1.6}$$

If we represent the received waveform as a delayed and scaled version of the transmitted signal $x_r(t) = ax(t - t_d)$, this becomes

$$y(t) = a\int_{-\infty}^{\infty} h(t-\tau)x(\tau - t_d)d\tau. \tag{1.7}$$

If the transmitted signal $x(t)$ is known, the matched filter is given by the complex conjugated of the time-reversed signal. This is known to maximise the output SNR in the presence of white noise [11]:

$$h(t) = x^*(-t), \tag{1.8}$$

Substituting this gives

$$y(t) = a \int_{-\infty}^{\infty} x^*(\tau - t)x(\tau - t_d)d\tau, \tag{1.9}$$

which maximises the output $y(t)$ for $t = t_d$

$$\max_t |y(t)| = y(t_d) = a \int_{-\infty}^{\infty} |x(\tau - t_d)|^2 d\tau = a \int_{-\infty}^{\infty} |x(\tau)|^2 d\tau \tag{1.10}$$

and the peak in $y(t)$ is proportional to the energy of the signal $x(t)$. Here, a is a positive scalar and has no influence on the performance of the matched filter. Below, a derivation of the matched filter is shown (adopted from [12]), to provide an explanation for the SNR and gain of a matched filter.

The spectrum of $x(t)$ is defined via the Fourier transform

$$X(f) = \int_{-\infty}^{\infty} x(t)e^{-j2\pi ft}dt, \tag{1.11}$$

and the spectrum of the matched filter is

$$H(f) = \int_{-\infty}^{\infty} x^*(-t)e^{-j2\pi ft}dt = X^*(f). \tag{1.12}$$

Using the fact that convolution in time domain leads to multiplication in the frequency domain, Eq. 1.6 can be written in the frequency domain as

$$Y(f) = H(f)X_r(f) = H(f)X(f)e^{-j2\pi ft_d}, \tag{1.13}$$

and taking the inverse Fourier transform to obtain

$$y(t) = \int_{-\infty}^{\infty} H(f)X(f)e^{j2\pi f(t-t_d)}df. \tag{1.14}$$

With additive white noise $n(t)$ at the input, the noise power spectrum (single-sided) is constant $N(f) = N_0$, so the noise power at the output of the matched filter is given by

$$\mathbb{E}[|y_n(t)|^2] = N_0 \int_{-\infty}^{\infty} |H(f)|^2 df. \tag{1.15}$$

Then, the SNR of the matched filter output at the peak ($t = t_d$) is

$$SNR = \frac{|y(t_d)|^2}{\mathbb{E}[|y_n(t)|^2]} = \frac{|\int_{-\infty}^{\infty} H(f)X(f)df|^2}{N_0 \int_{-\infty}^{\infty} |H(f)|^2 df}. \tag{1.16}$$

From the Schwartz inequality it is known that

$$|\int_{-\infty}^{\infty} H(f)X(f)df|^2 \leq (\int_{-\infty}^{\infty} |H(f)|^2 df) \cdot (\int_{-\infty}^{\infty} |X(f)|^2 df), \tag{1.17}$$

which implies that the SNR is bounded by

$$SNR \leq \frac{1}{N_0} \int_{-\infty}^{\infty} |X(f)|^2 df = \frac{E}{N_0}, \tag{1.18}$$

where $E = \int_{-\infty}^{\infty} |X(f)|^2 df = \int_{-\infty}^{\infty} |x(t)|^2 dt$ is the energy of $x(t)$. Eq. 1.18 holds with equality for $H(f) = X^*(f)$, which therefore maximises the SNR at the output of the filter. Interestingly, the matched filter output SNR is seen to be independent of bandwidth. This might seem contradicting at first, since increasing the bandwidth should lead to more noise power. Indeed, this is true for the input SNR of the matched filter, which is given in terms of power as

$$SNR_{in} = \frac{P_x}{P_n} = \frac{E/T}{N_0 B}, \tag{1.19}$$

where B is the bandwidth of the received signal. Then the ratio of the output to input SNR is the gain of the matched filter (the processing gain in Eq. 1.2.1)

$$G = \frac{SNR_{out}}{SNR_{in}} = BT. \tag{1.20}$$

If the bandwidth of the received signal is increased, the decrease in input SNR is compensated by the increase in gain achieved by the matched filter. Therefore, the output SNR is independent of the bandwidth in the case of white noise as seen from Eq. 1.18. This means that if the power spectral density of the noise is fixed, the only way to improve the output SNR of the matched filter is to increase the total signal energy.

However, the bandwidth does have a determinate effect on the mainlobe and sidelobe structure produced by the matched filter, which generally improves with bandwidth in terms of peak-to-sidelobe levels. The width of the mainlobe is an indication of the achievable range resolution. The sidelobes are unwanted since the return of a strong target can produce sidelobes that have a larger amplitude than the main lobe of weaker targets at another range, thereby potentially masking them. The range resolution of a simple pulse of duration τ is defined as

$$\Delta R = \frac{c\tau}{2}, \tag{1.21}$$

which is the minimal difference in range measurable using that pulse. The bandwidth of the simple pulse is found by the inverse of the pulse duration $B = 1/\tau$. This is used to define the range resolution of a signal with bandwidth B and corresponds to the Rayleigh resolution, equivalent to 4 dB width in the matched filter response [13].

$$\Delta R = \frac{c}{2B}. \tag{1.22}$$

Therefore, in order to send longer pulses (high energy), we need to increase the bandwidth of the signal to improve the range resolution. This is a reason for using frequency modulated or phase modulated pulses, for which a few examples will be shown in the next section.

2 Moving target detection

This chapter aims to improve the detection capabilities of active sonar for a low SNR moving target using coherent integration over multiple pulses. Here only a single sensor is considered[1], being a microphone for the in-air experiments, and a hydrophone or sonar transducer for a harbour. This work could be used as the basis for a long-range diver detection sonar, which potentially uses multiple such sensors. While no explicit detector is proposed in this chapter, the methods of imaging serve as a preliminary to the detection of a moving target. There are two questions to be answered in this chapter:

1. *How to apply coherent integration over multiple pulses for moving target detection?*
2. *What is the optimal transmit waveform for detecting a moving target in a clutter dominated environment?*

A processing method for coherent integration over multiple pulses is proposed in section 2.2 as an answer to the first question. In attempt to answer the second question, two different types of waveforms are compared: pseudo-random noise (PRN) and frequency modulated sweeps (chirps). First, the waveforms are compared in section 2.1 based on their correlation properties in the presence of a Doppler shift (ambiguity function). In section 2.2, first a general signal model is given for the received signal of a (constant velocity) moving target, given an arbitrary transmit waveform. Then, the signal is demodulated to baseband and split up in short time segments, over which the Doppler shift is assumed to be negligible, thereby simplifying the subsequent processing steps. Applying a short-time matched filter results in a signal model for targets in range-time, in which the ambiguity function of the transmit waveform comes back. The main reason for this approach is that the resulting range-time image can be analysed and interfering signals from static targets (clutter) can be more easily filtered out, as discussed in section 2.2.3. The 'traditional' method of moving target detection is discussed in section 2.2.4. To overcome the limitations of this method, a Radon-Fourier transform (RFT) is proposed in section 2.2.5. The RFT is shown to achieve coherent integration and is compared to a matched filter bank for moving targets in 2.3.1.

In section 2.3 the proposed method is tested using synthetic data of an ideal moving target, and the different waveforms are compared in terms of imaging performance. The methods are tested using the in-air demonstrator as seen in Figure 2.1, to see the effect of noise and clutter interference. Finally, the conclusions and some considerations for implementation in a realistic scenario are given in section 2.4.

[1] A single sensor, meaning a single receiver. If the transmit signal is continuous wave, then the source and receiver need to be on two separate elements, but for a pulsed signal the source and receiver can sometimes be implemented on the same element, such as a sonar transducer.

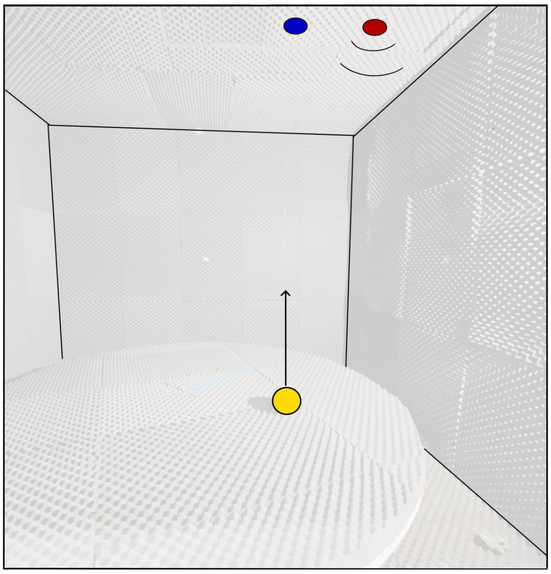

Figure 2.1: Schematic of the in-air demonstrator for moving target detection. The yellow bulb represents the moving target, which moves towards the receiver (blue) while reflecting the signal from the loudspeaker (red).

2.1 Ambiguity function

The type of waveform that is used in active sonar will affect the ability of the system to detect targets. It is therefore useful to study the resolution that a specified waveform has for estimating the range and Doppler of a target. As a rule of thumb, the range resolution improves proportionally to the bandwidth and the Doppler resolution improves with the time duration of the signal. The ambiguity function is the most used tool to inspect the correlation properties of a waveform and is the main focus of this section.

If the sonar system and the reflector are not at rest with respect to each other, the frequency of the echo will slightly differ from the incoming frequency due to the Doppler effect. The received frequency of a Doppler shifted signal is equal to

$$f_r = (\frac{1 + v/c}{1 - v/c})f = \eta f, \tag{2.1}$$

where c is the medium velocity and v is the radial velocity of the moving target towards the receiver. The compression factor η can be simplified by writing the denominator as a series, so that:

$$\eta = (1 + v/c)[1 + (v/c) + (v/c)^2 + \dots] = [1 + 2(v/c) + 2(v/c)^2 + \dots]. \tag{2.2}$$

In radar and sonar the targets usually move at a small fraction of the medium velocity $v/c \ll 1$ and the expression is simplified by discarding the second-order and higher order terms [11]. The Doppler frequency is therefore approximated by the frequency difference of the incoming signal and the echo as

$$f_D = (\eta - 1)f \approx \frac{2v}{c}f = \frac{2v}{\lambda}. \tag{2.3}$$

If the received signal contains a Doppler shift and is left uncompensated, this could result in a loss of the matched filter output. This effect is studied using the wide-band ambiguity function (WAF), which is given by the 2D-correlations over delay and Doppler scaling [14]:

$$\chi(\tau, \eta) = \sqrt{\eta} \int_{-\infty}^{\infty} s(t)s^*(\eta(t-\tau))dt. \tag{2.4}$$

Under the narrowband assumption the WAF reduces to the (Woodward's) ambiguity function [15]:

$$\chi_{\mathrm{NB}}(\tau, f_D) = \int_{-\infty}^{\infty} s(t)s^*(t-\tau)e^{j2\pi f_D t}dt. \tag{2.5}$$

Since the frequency range dealt with in this thesis are mostly considered wideband, the proposed signals shall be investigated using the WAF. To be able to compare the peak to sidelobe ratio of different waveforms it is useful to apply a normalisation, such that the maximum value at zero delay and zero Doppler ($v = 0$, so $\eta = 1$) is unity $|\chi_n(0,1)| = 1$. The normalized WAF is then defined as

$$\chi_n(\tau, \eta) = \frac{\chi(\tau, \eta)}{||x(t)||^2} = \frac{\chi(\tau, \eta)}{\chi(0,1)}. \tag{2.6}$$

2.1.1 Frequency modulated waveforms

A common pulse modulation technique is frequency modulation, which is a sinusoid that increases or decreases its frequency over time. The simplest and most common example is linear frequency modulation (LFM), leading to a linear chirp. The LFM waveform can be represented by the complex exponential

$$s(t) = e^{j\left(2\pi(f_1 t + \frac{1}{2}kt^2) + \phi_0\right)}, \quad 0 \leq t \leq T. \tag{2.7}$$

Here ϕ_0 is the phase at $t = 0$ and $k = \frac{f_2 - f_1}{T}$ is the sweep rate, based on the lower and upper frequencies. For an FM signal with $f_1 < f_2$, the frequency sweeps from f_1 to f_2 during time period T.

Using Euler's equation we can represent a sinusoidal signal as the real part of the complex exponential since

$$Re\{e^{j\phi(t)}\} = Re\{cos(\phi(t)) + jsin(\phi(t))\} = cos(\phi(t)), \tag{2.8}$$

where $\phi(t)$ is the phase of the signal, whose instantaneous frequency is $f(t) = \frac{1}{2\pi}\frac{d\phi(t)}{dt}$. Therefore, the instantaneous frequency of the LFM waveform is given by

$$f(t) = \frac{1}{2\pi}\frac{d}{dt}\left(2\pi(f_1 t + \frac{1}{2}kt^2) + \phi_0\right) = f_1 + kt. \tag{2.9}$$

For wideband signals, hyperbolic frequency modulation (HFM) is often used, which is represented by

$$s(t) = e^{j\left(\frac{2\pi}{b} ln(1+bf_1 t)+\phi_0\right)}, \quad 0 \leq t \leq T, \tag{2.10}$$

where $b = (f_1 - f_2)/(f_1 f_2 T)$. The instantaneous frequency is then given by

$$f(t) = \frac{1}{2\pi}\frac{d}{dt}\big(\frac{2\pi}{b} ln(1 + bf_1 t) + \phi_0\big) = \frac{f_1}{1 + bf_1 t}. \tag{2.11}$$

2.1.1.1 Doppler tolerance of frequency modulated waveforms

Doppler tolerance refers to the property of a waveform to maintain its shape, despite the frequency changes that occur from the Doppler effect. The HFM pulse has the property that a Doppler shifted version of the signal can be represented by a time shifted version of the pulse, which is also called a Doppler-invariant property [16]. This property holds under the assumption that the target has a constant radial velocity. The HFM pulse is in this case maximally Doppler tolerant, since correlation of a Doppler shifted echo with the transmitted pulse is maintained. The received echo of a moving target can be represented as

$$r(t) = a\sqrt{\eta}s\big(\eta(t - \tau)\big), \tag{2.12}$$

where $\tau = \frac{2R}{c}$ is the delay of the two-way propagation to the target at range R, η is the Doppler scaling factor given by Eq. 2.1 and a is an amplitude scaling factor.

Applying this shift to the HFM signal of Eq. 2.10 (assuming $\phi_0 = 0$) gives

$$r(t) = a\sqrt{\eta}e^{j\frac{2\pi}{b} ln(1+bf_1(\eta(t-\tau))}. \tag{2.13}$$

The instantaneous frequency of the Doppler-shifted received pulse is

$$f_D(t) = \frac{d}{dt}\big(\frac{1}{b} ln(1 + bf_1(\eta(t - \tau)))\big) = \frac{f_1\eta}{1 + bf_1\eta(t - \tau)}, \tag{2.14}$$

whereas the frequency of the transmitted pulse is given by

$$f(t) = \frac{f_1}{1 + bf_1(t - \tau)}. \tag{2.15}$$

To show that the HFM pulse satisfies the Doppler-invariant property for a given time shift t_0, we can equate

$$f_D(t) = f(t - t_0), \tag{2.16}$$

which by substitution gives

$$\frac{f_1\eta}{1 + bf_1\eta(t - \tau)} = \frac{f_1}{1 + bf_1(t - t_0 - \tau)}. \tag{2.17}$$

Then solving for t_0 leads to a constant

$$t_0 = \frac{(\eta - 1)}{\eta b f_1} = \frac{(\eta - 1) f_2 T}{\eta (f_1 - f_2)}, \tag{2.18}$$

which shows that the Doppler shifted HFM pulse is equivalent to the original pulse, shifted in time by a constant t_0. This effect, commonly termed range-Doppler coupling, is generally unwanted, but is a compromise with Doppler insensitivity [17]. For a target with a positive radial velocity (moving towards the receiver), $\eta > 1$ and $f_2 > f_1$ gives a negative time shift $t_0 < 0$. Therefore, after directly applying a matched filter, this target appears closer than it actually is.

Repeating this procedure for LFM shows that the time shift needed to satisfy Eq. 2.16 includes a time dependency, showing that the Doppler shifted LFM signal is not equivalent to a (constant) time shifted version. However, HFM will approach LFM if the signal is sufficiently narrowband. From a series expansion of the HFM frequency function we get

$$f(t) \approx \Big[\frac{f_1}{1 + b f_1 t'} - \big(\frac{b f_1^2}{(1 + b f_1 t')^2}\big)(t - t') + \big(\frac{b^2 f_1^3}{(1 + b f_1 t')^3}\big)(t - t')^2 + \ldots\Big]_{t'=0}, \tag{2.19}$$

where: $b = (f_1 - f_2)/f_1 f_2 T$. The terms including $b^2, b^3, \cdots$ are approximately zero for narrowband frequencies, thus reducing to

$$f(t) \approx f_1 - b f_1^2 t = f_1 - \frac{f_1 - f_2}{f_1 f_2 T} f_1^2 t \approx f_1 + \frac{f_2 - f_1}{T} t, \tag{2.20}$$

which is the expression for LFM. Therefore, LFM is equivalently Doppler tolerant under the assumption that the signal is narrowband, i.e. the centre frequency $f_c = (f_1 + f_2)/2$ is much higher than the bandwidth $B = f_2 - f_1$. However, since the low-to-medium frequency pulses considered in this thesis are not necessarily narrowband, HFM is preferred.

The wideband ambiguity function for the proposed frequency modulated waveforms is not easily derived. Therefore, the WAF is analysed numerically, by computing the Doppler shifted signals and correlating them to the original. As example, the normalised WAF given by Eq. 2.6, are shown for LFM and HFM pulses of 1 second duration in Figure 2.2. From the WAF of LFM it is seen that both the correlation gain and the mainlobe resolution degrades for echoes with an increased Doppler shift.

2.1.2 Pseudo-random waveforms

Another common type of pulse modulation is phase modulation, for which one of the simplest forms is binary phase modulation, or binary phase shift keying (BPSK) as used in communications. The waveform consists of a random binary sequence modulated on a carrier, where the bitrate determines the bandwidth of the waveform. BPSK pulses have been previously considered for long-range low-frequency active sonar [18], mainly due to their ability to unambiguously identify a target echo in both range and Doppler using a single pulse. The BPSK waveform is given by the complex exponential

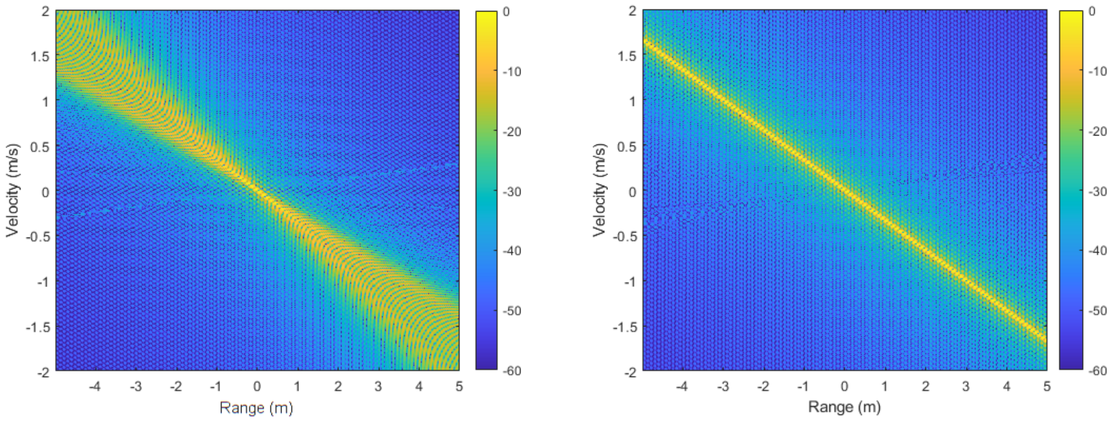

(a) LFM (b) HFM

Figure 2.2: Normalised wideband ambiguity function $|\chi_n(\tau,\eta)|^2$ in dB for a single pulse of LFM and HFM, with a duration of 1 second, with $B = |f_2 - f_1| = 5$ kHz bandwidth and $f_c = 12.5$ kHz centre frequency.

$$s(t) = e^{j\left(2\pi f_c t + \theta_b(t) + \phi_0\right)}, \quad 0 \leq t \leq T. \tag{2.21}$$

Here $\theta(t)$ is the binary signal alternating between $0, \pi$ and f_c is the carrier frequency. The ambiguity function for BPSK with a random binary sequence is almost identical to white noise that is bandpass filtered over the same bandwidth. Bandpass filtered noise is therefore expected to have similar performance to the BPSK waveform, but BPSK could be preferred since it is more easily generated in hardware. However, both have similar correlation performance and will therefore be referred to as pseudo-random noise (PRN) in the rest of this thesis.

The SNR gain of a PRN waveform after applying pulse compression is equal to BT, which for a random binary phase coded waveform is equal to $F_bT = N$, the number of bits, for a given bitrate F_b and signal duration T. The peak amplitude increases with BT due to coherent integration, whereas the sidelobe level increases with $\sqrt{BT}$ (non-coherent integration). This means that the peak-to-sidelobe ratio improves with the duration of the signal. This is not the case for frequency modulated waveforms, which stretch out in time if the duration of a single chirp is increased. The normalised WAF for 1 second of PRN (using random BPSK) is shown in Figure 2.3. The resolution of this waveform in Doppler is said to be almost identical to the CW signal with the frequency of the carrier [19], for which the 4-dB (in amplitude) resolution is $\Delta v = \frac{c}{f_c T}$.

From the ambiguity function in Figure 2.3, it is observed that the PRN waveform is not Doppler-tolerant, as opposed to the frequency modulated waveforms. The advantage is that a moving target can be uniquely identified in both range and velocity using a single pulse, as there is no coupling between range and Doppler. However, a relatively high level of sidelobes is obtained over the entire range-Doppler domain of the pulse. The width of the mainlobe in range and velocity is given by $\Delta R = \frac{c}{2B}$ and $\Delta v = \frac{c}{f_c T}$, respectively. The autocorrelation sidelobes for HFM and PRN are compared in Figure

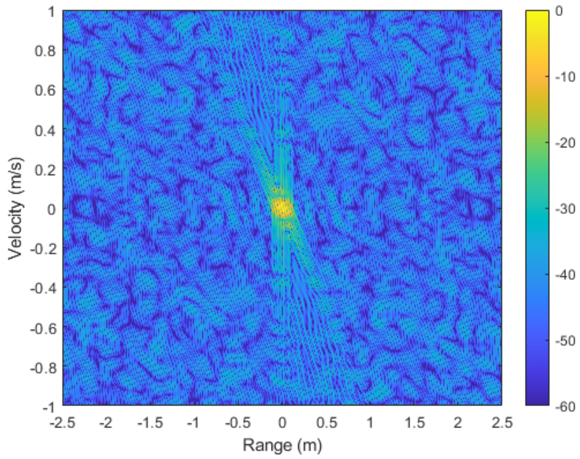

Figure 2.3: Normalised wideband ambiguity function $|\chi(\eta, \tau)|^2$ for 1 second of PRN (random BPSK) waveform with $B = 5$ kHz and $f_c = 12.5$ kHz carrier frequency. Observed is a single mainlobe plus sidelobe plateau in range-Doppler.

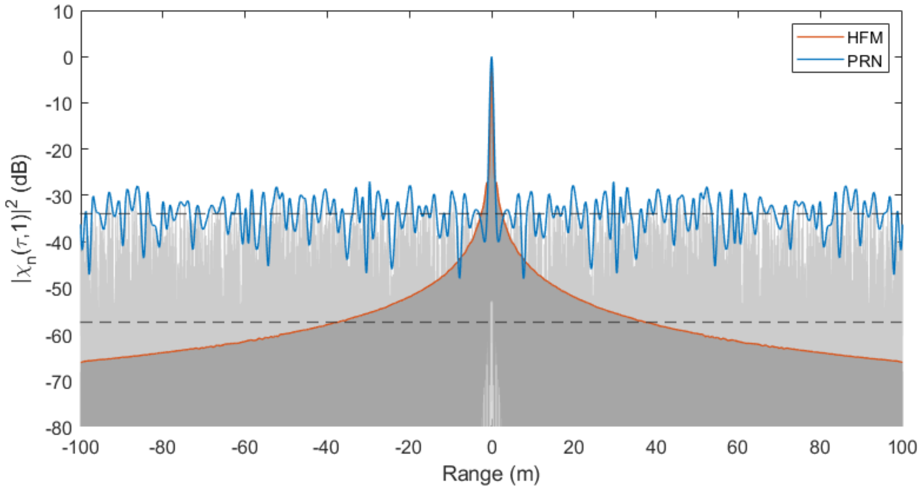

Figure 2.4: A comparison of the autocorrelation of PRN and HFM. Both pulses are 1 second long, with a carrier frequency of 12.5 kHz and 5 kHz bandwidth. The coloured lines represent the envelope of the peaks in the autocorrelation. From the peak envelope, the average sidelobe level is computed in the region outside of the 4-dB mainlobe, and is shown by the dashed lines. The average peak level of the sidelobes for the PRN pulse is -34 dB and -57 dB for the HFM pulse.

2.4, which is the zero-Doppler cut of their ambiguity function. Noticeably, the range sidelobes of HFM are much lower than that of PRN for a pulse of 1 second duration. A similar sidelobe level for PRN is obtained when the signal duration is increased to over 100 seconds.

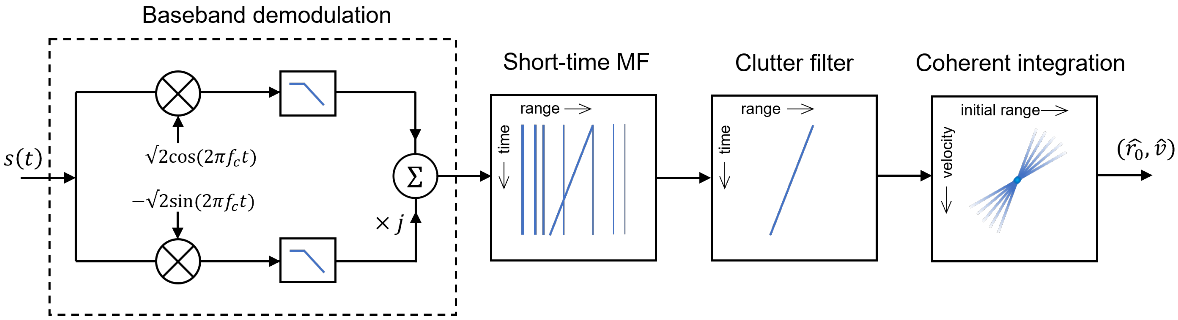

Figure 2.5: Pipeline of the proposed processing method. The individual blocks in this figure are explained in the next subsections.

2.2 Coherent integration of moving target signals

In this section, a processing algorithm is proposed for detecting a low SNR moving target. The detection algorithm itself is beyond the scope of this thesis, but should be a straightforward extension. To ensure the detectability of a low SNR target, a long integration time might be required, potentially extending to many pulse durations. This requires an accurate model of the target's signal, which could be difficult to obtain, as the motion of the target is generally unknown. To address this problem, we assume that over a certain period of time, the target's motion can be accurately modelled with a constant radial velocity towards the sensors. The trajectory of the target over this interval can then be described by two parameters: *initial range* and *velocity*, which we aim to estimate.

First, the signal model of a moving target in baseband is derived in section 2.2.1. There are two reasons for processing baseband signals: to reduce the computational cost, as we can often down-sample, and to measure the phase of the signal. Secondly, the signal is split up in short time-segments, over which the target's movement is negligible. We can then apply a matched filter for static targets, below named the 'short-time matched filter', which simplifies the processing and allows for a method to image in range-time. This intermediate stage, is used to separate the target signal from the clutter. The final step is to integrate the signal of the target in range-time, knowing the phase changes and range walk that correspond to a certain initial range and velocity.

In Figure 2.5, the proposed processing pipeline is shown, which follows the same order as the coming subsections and should therefore give a clearer picture of how the individual methods are combined. The first step in the processing algorithm is to demodulate the measured signal $s(t)$ to baseband, after which a low-pass filter is applied. The complex baseband data is then split up in a fast-, slow-time matrix and a matched filter (for static targets) is applied to obtain a range-time image. On the output of the matched filter, the clutter filter is applied, which is implemented with an MTI filter and/or CLEAN, as explained in section 2.2.3. The final step is integration from the range-time image, which is implemented with the Radon-Fourier transform, as explained in section 2.2.5. In section 2.3.1, the proposed method is compared against a matched filter bank for constant velocity targets.

2.2.1 Signal model of a moving target

In this section, the baseband signal model of a moving target is shown. This model is later used to derive the short-time matched filter for a moving target. A complete derivation of the short-time matched filter was not found and is therefore provided in section 2.2.2 with intermediate steps, using the work of N. Petrov [20] as a basis.

Consider the transmit waveform, which is given by the real part of the complex envelope $g(t)$ modulated by a carrier at frequency f_c, as

$$s_T(t) = Re\big\{g(t)e^{j2\pi f_c t}\big\}, \quad 0 \leq t \leq T, \tag{2.22}$$

for a transmission of length T (in seconds). If this transmission is reflected from a point target at range r_0, the delay of its echo is given by $\tau = 2r_0/c$. Writing the received signal as a scaled and delayed version of the transmission then gives

$$s_r(t) = as_T(t-\tau) = Re\{ag\big(t - \frac{2r_0}{c}\big)e^{j2\pi f_c(t-\frac{2r_0}{c})}\}. \tag{2.23}$$

The complex baseband signal is obtained by multiplying the complex signal

$$s_{r,bb}(t) = a\big(g(t-\tau)e^{j2\pi f_c(t-\tau)}\big)e^{-j2\pi f_c t} = ag(t-\tau)e^{-j2\pi f_c \tau}, \tag{2.24}$$

writing $f_c\tau = f_c\frac{2r_0}{c} = \frac{2r_0}{\lambda}$, where λ is the wavelength of the carrier, gives the received signal in complex baseband for a static target

$$s_{r,bb}(t) = ag\big(t - \frac{2r_0}{c}\big)e^{-j4\pi\frac{r_0}{\lambda}}. \tag{2.25}$$

From this expression it is seen that in baseband, a delayed signal is a time shifted version of the baseband signal $g(t)$ with an additional phase shift of the carrier. This is used in chapter 3 to derive the matched filter for imaging from the baseband signal.

Suppose that there is a moving target whose range is given by its initial range r_0 and constant radial velocity v towards the sensors, as

$$r(t) = r_0 - vt, \quad 0 \leq t \leq T. \tag{2.26}$$

We can find the echo delay τ as a function of time by realising that a signal received at time t reflected from the moving target at time $t - \frac{\tau}{2}$. Then $\tau(t)$ is found by solving for the two-way propagation distance [21]

$$c\tau(t) = 2\big(r_o - v(t - \frac{\tau(t)}{2})\big), \tag{2.27}$$

$$\tau(t) = \frac{2(r_0 - vt)}{c - v}, \tag{2.28}$$

which is approximated by

$$\tau(t) = \frac{2(r_0 - vt)}{c}, \tag{2.29}$$

under the condition that the target radial velocity is low compared to the medium velocity $v/c \ll 1$, which is assumed in the following derivations. Substituting this expression for $\tau(t)$ in Eq 2.24 leads to the following expressions for the received signal of a moving target

$$s_r(t) = Re\{ag\big((1+\frac{2v}{c})t - \frac{2r_0}{c}\big)e^{j2\pi f_c(t(1+\frac{2v}{c})-\frac{2r_0}{c})}\}, \tag{2.30}$$

and its baseband representation

$$s_{r,bb}(t) = ag\big((1+\frac{2v}{c})t - \frac{2r_0}{c}\big)e^{j2\pi f_c(\frac{2v}{c}t-\frac{2r_0}{c})}. \tag{2.31}$$

From this equation we see that the received signal is a copy of the transmit signal with a time dilation or compression $(1+\frac{2v}{c})$ and a frequency shift, due to the Doppler effect. The exponential in the baseband expression can be written as the product of a time-varying phase shift and a constant $e^{j2\pi f_c(\frac{2v}{c}t-\frac{2r_0}{c})} = e^{j2\pi(\frac{2v}{\lambda})t}e^{-j4\pi\frac{r_0}{c}}$, where $\frac{2v}{\lambda} = f_D$ is the Doppler frequency of the carrier. Including the phase and attenuation constants in a new (complex-valued) constant α gives

$$s_{r,bb}(t) = \alpha g\big((1+\frac{2v}{c})t - \frac{2r_0}{c}\big)e^{j2\pi f_c\frac{2v}{c}t}. \tag{2.32}$$

In pulsed radar and sonar systems, the measured signal is split up in fast-time (time within one pulse duration) and slow-time (from pulse to pulse). Adopting this method, we define fast time as $t' = t - mT_w$ with $t' \in [0, T_w]$, such that $\tau(t) = \tau(t' + mT_w)$, where $m = 0, 2\dots M-1$ is slow-time. The baseband signal can then be written as [20]

$$s_{r,bb}(t', m) = ag\big(t' - \tau(t' + mT_w)\big)e^{-j2\pi f_c\tau(t'+mT_w)}. \tag{2.33}$$

Using Eq. 2.29, $\tau(t' + mT_w) = \frac{2r_0}{c} - \frac{2v(t'+mT_w)}{c}$, substituting this gives

$$s_{r,bb}(t', m) = ag\big((1+\frac{2v}{c})t' + \frac{2v}{c}mT_w - \frac{2r_0}{c}\big)e^{j2\pi f_c\left(\frac{2v}{c}(t'+mT_w)-\frac{2r_0}{c}\right)}. \tag{2.34}$$

Here the time length of a window T_w is chosen such that the radial displacement of the target within the duration of the window is below the range resolution: $|vT_w| \ll \Delta R$. It is thus assumed that over a short period of time the target is static. However, the targets movement over multiple of such windows (slow-time) cannot be neglected and is referred to as range migration.

Under the assumption that the target is static in fast-time, the time dilation of the complex envelope in fast-time can be neglected:

$$s_{r,bb}(t', m) \approx \alpha g(t' + \frac{2v}{c}mT_w - \frac{2r_0}{c})e^{j2\pi f_c\left(\frac{2v}{c}(t'+mT_w)\right)}. \tag{2.35}$$

This means that in fast-time the received baseband signal is a delayed version of the transmit baseband signal with $\tau = \frac{2r_0}{c} - \frac{2v}{c}mT_w$, scaled with a complex-valued constant, and multiplied with the phase term $e^{j2\pi f_c(\frac{2v}{c}(t'+mT))}$. We can then apply a matched filter over fast-time (which is translated to range) for each slow-time sample (giving time) to obtain a range-time image. This approach is explained and derived below in section 2.2.2. Applying this rearrangement of the signal is obvious when sending repetitive pulses with a fixed pulse repetition interval (PRI), as these have inherent range ambiguities. However, here the procedure is applied to continuous transmit waveforms as well. The main reason for applying this signal rearrangement to PRN is that it allows for more flexibility in the processing, as we can choose any window length T_w. The other reason is that the intermediate domain of range-time makes sense intuitively, and can be used to separate the moving target signal and clutter interference.

2.2.2 Short-time matched filter

In this section, a matched filter for static targets (see section 1.2.2) is applied to each fast-time window from Eq. 2.35. This approach is 'matched' over a short period of time, during which the motion of the target is assumed to be negligible, hence the name short-time matched filter. Below, we derive the short-time matched filter response of a moving target as a function of the transmit signal in baseband. This can be implemented using linear convolution of the signals in time, or using their Fourier transform, as shown below, which achieves circular convolution. Both can be used, but it is important to note that the latter requires zero-padding of the time domain sequences in order to achieve the same result as linear convolution. For CW PRN, the linear convolution is extended to the next window to avoid losses due to edge effects.

Using the frequency domain notation, given in Eq. 1.12, the matched filter can be written as an inverse Fourier transform:

$$s_{MF}(t', m) = \int S_{r,bb}(f, m) G^*(f, m) e^{j2\pi f t'} df, \tag{2.36}$$

where $S_{r,bb}(f, m)$ and $G(f, m)$ are the Fourier transform of $s_{r,bb}(t', m)$ and $g(t', m)$, respectively. Using the expression from Eq. 2.35, $S_{r,bb}(f, m)$ is given by

$$\begin{aligned} S_{r,bb}(f, m) &= \int_{t'=0}^{T_w} s_{r,bb}(t', m) e^{-j2\pi f t'} dt' \\ &= \alpha e^{j2\pi f_c (\frac{2v}{c}) m T_w} \int g\big(t' + \frac{2v}{c} m T_w - \frac{2r_0}{c}\big) e^{j2\pi f_c (\frac{2v}{c}) t'} e^{-j2\pi f t'} dt'. \end{aligned} \tag{2.37}$$

This integral is first simplified by the following substitution:

$$t' = t'' - (\frac{2v}{c} m T_w - \frac{2r_0}{c}), \quad dt' = dt'', \tag{2.38}$$

so that the integral term in Eq. 2.37 is written as

$$\begin{aligned}
&\int g\big(t' + \frac{2v}{c}mT_w - \frac{2r_0}{c}\big)e^{j2\pi f_c(\frac{2v}{c})t'}e^{-j2\pi f t'}dt' \\
&= \int g(t'')e^{j2\pi f_c(\frac{2v}{c})(t'' - \frac{2v}{c}mT_w + \frac{2r_0}{c})} \cdot e^{-j2\pi f(t'' - \frac{2v}{c}mT_w + \frac{2r_0}{c})}dt'' \\
&= \int g(t'')e^{j2\pi f_c(\frac{2v}{c})(\frac{2r_0}{c} - \frac{2v}{c}mT_w)} \cdot e^{j2\pi f_c(\frac{2v}{c}t'')} \cdot e^{-j2\pi f(\frac{2r_0}{c} - \frac{2v}{c}mT_w)} \cdot e^{-j2\pi f t''}dt'' \\
&= e^{j2\pi(f_c\frac{2v}{c} - f)(\frac{2r_0}{c} - \frac{2v}{c}mT_w)}\int g(t'')e^{-j2\pi(f - f_c\frac{2v}{c})t''}dt'' \\
&= e^{j2\pi(f_c\frac{2v}{c} - f)(\frac{2r_0}{c} - \frac{2v}{c}mT_w)}G(f - f_c\frac{2v}{c}).
\end{aligned} \tag{2.39}$$

The Fourier transform of the received signal in baseband is therefore given by

$$S_{r,bb}(f,m) = \alpha e^{j2\pi f_c(\frac{2v}{c})mT_w}e^{j2\pi(f_c\frac{2v}{c} - f)(\frac{2r_0}{c} - \frac{2v}{c}mT_w)}G(f - f_c\frac{2v}{c}), \tag{2.40}$$

which simplifies because

$$e^{j2\pi(f_c\frac{2v}{c} - f)(\frac{2r_0}{c} - \frac{2v}{c}mT_w)} = \underbrace{e^{j2\pi f_c(\frac{4vr_0}{c^2} - (\frac{2v}{c})^2 mT_w)}}_{\approx 1,\text{ since } \frac{v}{c^2},\ \frac{v^2}{c^2} \approx 0.}e^{j2\pi f(\frac{2r_0}{c} + \frac{2v}{c}mT_w)} \approx e^{j2\pi\left(f(\frac{2v}{c}mT_w - \frac{2r_0}{c})\right)}, \tag{2.41}$$

finally giving

$$S_{r,bb}(f,m) \approx \alpha e^{j2\pi f_c(\frac{2v}{c})mT_w}e^{j2\pi f(\frac{2v}{c}mT_w - \frac{2r_0}{c})}G(f - f_c\frac{2v}{c}). \tag{2.42}$$

Substituting this expression in Eq. 2.36, gives the matched filter output:

$$\begin{aligned}
s_{MF}(t',m) &= \alpha e^{j2\pi f_c(\frac{2v}{c})mT_w}\int e^{j2\pi f(\frac{2v}{c}mT_w - \frac{2r_0}{c})}G(f - f_c\frac{2v}{c})G^*(f)e^{j2\pi f t'}df \\
&= \alpha e^{j2\pi f_c(\frac{2v}{c})mT_w}\int G(f - f_c\frac{2v}{c})G^*(f)e^{j2\pi f(t' + \frac{2v}{c}mT_w - \frac{2r_0}{c})}df \\
&= \alpha e^{j2\pi f_c(\frac{2v}{c})mT_w}\int G(f - f_c\frac{2v}{c})G^*(f)e^{j2\pi f t''}df \\
&= \alpha e^{j2\pi f_c(\frac{2v}{c})mT_w}\chi_{g,\mathrm{NB}}\big(t'', f_c\frac{2v}{c}\big),
\end{aligned} \tag{2.43}$$

in which we recognise the ambiguity function of the baseband transmit signal $g(t',m)$ (the last step is derived in appendix A), centred at $t'' = t' - (\frac{2r_0}{c} - \frac{2v}{c}mT_w) = t' - \tau(m)$. Furthermore, we can use that $f_c\frac{2v}{c} = f_D$ is the Doppler frequency, to get

$$s_{MF}(t',m) = \alpha e^{j2\pi f_D mT_w}\chi_{g,\mathrm{NB}}\big(t' - \tau(m), f_D\big). \tag{2.44}$$

Note that this result is obtained if for each short-time window, the baseband transmission $g(t)$ is the same (e.g. for repetitive pulses). However, it might be that the transmission signal is different in each window. This is the case for PRN, or when processing in windows shorter than the pulse duration: $T_w < T_p$. To indicate that the ambiguity function of every short-time segment can be different, a slow-time subscript is added to the AF:

$$s_{MF}(t', m) = \alpha e^{j2\pi f_D m T_w} \chi_{g_m,\mathrm{NB}}\big(t' - \tau(m), f_D\big). \tag{2.45}$$

From this expression we see that output of the matched filter in baseband represents a slice of the 2D AF of that short-time segment at a specific f_D, multiplied with a phase term that changes in slow-time, corresponding to the Doppler shift of the carrier. Note that here the narrowband ambiguity function is obtained (as in Eq. 2.5). This means that the output of the matched filter in baseband for short window m is approximated by the narrowband ambiguity function, under the made assumption that the target velocity is relatively low $v/c \ll 1$.

2.2.3 Clutter suppression

In practise, the transmitted signal will reflect not only from the moving target, but also from the (static) reflectors present in the surrounding. These static or slowly moving reflectors are called clutter and will interfere with the signal of the moving target if received simultaneously. The sidelobes can potentially mask the target if the clutter signal is much stronger than the target signal. The simplest way of tackling this is by introducing gaps in the transmission, or silent-periods, so that the clutter and target signal do not overlap in time.

Considering a CW PRN transmit signal for higher SNR gain, we have to assess whether the target signal could come above the clutter interference level, given a certain integration time. In the case of a continuous transmission, sending and receiving has to be done from two separate nodes. The strongest interference signal is then normally the direct-path interference from the transmitter. The direct-path is expected to be truly static, and could likely be filtered out. However, there might be components that have a low Doppler shift, such as the reflections from the moving sea surface, whose echoes might not be easily removed from the measured signal, and will thus contribute to sidelobes over the whole range domain.

As seen in section 2.1.2, the peak-to-sidelobe ratio for PRN improves with the BT-product. Assuming we can coherently integrate a target signal, having a power of P_{target}, the integration time needed for the integrated target signal to come above the sidelobe level of the clutter (having a power $P_{clutter}$) is

$$BT_{int} \cdot P_{target} > P_{clutter}, \quad T_{int} > \frac{P_{clutter}}{B \cdot P_{target}}. \tag{2.46}$$

This gives the minimum integration time that is needed to detect a target in the presence of an uncompensated clutter signal. If this condition is not satisfied after clutter filtering, then the target will be masked by sidelobes. Therefore, satisfying this condition is necessary in order for a CW transmission to have an advantage, independent of the level of noise. This is further discussed in section 2.4, in the context of the sonar equation for a realistic target detection scenario.

MTI filter

A moving target indication (MTI) filter, also called a pulse canceller, is used to suppress the static components in the pulsed compressed echoes. It is assumed that the measured signal is a superposition of echoes from the clutter and from the moving target. The clutter signal is expected to be the same for two consecutive echoes, however, the signal of the moving target has undergone a phase shift over one PRI. This motivates the simplest MTI, also called a two-pulse canceller, which takes the difference of the matched filter output $s_{MF}(t', m)$ over two successive slow-time samples [22].

The filter is described by the transfer function $H(z) = 1 - z^{-1}$, where $z = e^{j2\pi f_n}$ and $f_n = fT_w \in [-0.5,\ 0.5]$ is the normalised frequency corresponding to the Nyquist frequency range $[-PRF/2,\ PRF/2]$. The frequency response of the filter is then

$$H(f) = (1 - e^{-j2\pi fT_w}) = e^{-j\pi fT_w}(e^{j\pi fT} - e^{-j\pi fT_w}) = 2je^{-j\pi fT_w} sin(\pi fT_w). \tag{2.47}$$

The magnitude of this frequency response, $|H(f)| = |2sin(\pi fT_w)|$, shows a high-pass behaviour, having a null at zero frequency to suppress the clutter and two maxima at $f = \pm PRF/2$. For a moving target with a Doppler frequency $f < PRF/2$, the clutter suppression for the two-pulse canceller is accompanied by an attenuation of the target signal. Therefore, a higher order MTI filter could be designed, having a more flat pass band response, or a wider clutter suppression band.

An MTI filter can also be implemented in the time domain (i.e., before pulse compression), if the transmit signal is identical for each pulse. However, if the transmit signal varies in each window, such as in the case of PRN, then applying an MTI filter can only be done after pulse compression, which would only filter out the main lobe of the clutter and not the sidelobes. Therefore, MTI is suggested as a clutter filter for the chirps (HFM pulses) since they are identical each pulse.

CLEAN

CLEAN is a deconvolution algorithm, originally proposed for improving radio astronomy images. However, identically titled methods for removing clutter interference have been proposed in radar literature (e.g., in [23]) and are used in this section. In this section CLEAN is implemented in time-domain as a serial subtraction of the estimated clutter signals. It is assumed that the clutter signal can be represented as a delayed and attenuated version of the transmitted signal. By finding the highest peaks in the matched filter for static targets, we can estimate the delay at which these signals are received and subtract them from the measured signal. Since the moving target will not correlate at one single range, the target signal will be likely not affected. The drawback is that the algorithm should stop at the point the clutter signal strength is similar to that of the moving target, thereby potentially not suppressing weak clutter signals.

The algorithm can be summarised by a series of subtractions in time-domain, giving one iteration of CLEAN for the received signal $y(n)$ as:

$$y^{(k+1)}(n) = y^{(k)}(n) - \hat{A}_\tau x(n - \tau), \tag{2.48}$$

given a transmit signal $x(n)$, where the amplitude A_τ corresponds to the signal component at delay τ in the cross-correlation: $r_{yx}(\tau) = \sum_{n=0}^{N-1} y(n)x(n-\tau)$. This amplitude can be estimated by the correlation amplitude if we assume that this was the only component contributing to the correlation: $r_{yx} = \sum_{n=0}^{N-1} A_\tau x^2(n)$. However, if we have multiple signals at different delays, then the signal will have contributed only partly we should apply a scaling $0 < \alpha < 1$:

$$\hat{A}_\tau = \frac{\alpha r_{yx}(\tau)}{\sum_{n=0}^{N-1} x^2(n)} = \frac{\alpha r_{yx}(\tau)}{||x||^2}. \tag{2.49}$$

The procedure should be repeated until an appropriate stopping-criteria is met, for example, stop after the energy in the CLEAN signal is not significantly decreasing anymore per iteration. In the context of our signal model, $y(n)$ is a sampled version of the receive signal $s_t(t)$ and $x(n)$ a sampled version of the transmit signal $s_T(t)$.

CLEAN is proposed for processing PRN, to estimate and then subtract (in time-domain) the interference of the direct-path and clutter signal. Using an MTI filter after pulse compression would, in the case of PRN, only suppress the peaks of the clutter signals. However, applying an MTI filter after the CLEAN procedure could help remove any remaining clutter main-lobes, which is verified in the example shown below.

In Figure 2.6, the results of a moving target experiment in the in-air demonstrator are shown. The transmit waveform is CW PRN, which is sampled synchronously with the received signal at $F_s = 48$ kHz (measurement setup is described in section 2.3.2). The short-time matched filter $s_{MF}(t', m)$ is shown in (a), where multiple straight lines (constant range over time) are observed. These are the main-lobes of the clutter interference, which is in this case the static reflections in the room. The first line at approximately 0.75 m corresponds to the direct-path interference from transmitter to receiver. In (b) the MTI filter, in this case a two-pulse canceller, is applied on the short-time matched filter $s_{MF}(t', m)$. The main-lobes of the static reflections are suppressed, and the target track is revealed, however, the sidelobe levels are not reduced. In (c), CLEAN is applied using 2000 iterations, which removes most of the clutter interference and thereby reduces the sidelobe level by about 6 dB. In (d), both CLEAN and the MTI filter are applied, which appears to give the best performance in terms of imaging the moving target in the case of PRN.

2.2.4 Traditional moving target detection

The traditional processing method for moving target detection in radar is pulse-Doppler processing, which aims to extract the pulse-to-pulse phase change of the pulsed compressed signals over some coherent processing interval (CPI) [22]. In this section, we utilise pulse-Doppler processing on the range-time image ($s_{MF}(t', m)$ as given in section 2.2.2). It is important to note that pulse-Doppler processing is typically applied to pulsed signals only, but is here applied to either pulsed- or CW signals. The method is applied below, from which it is concluded that it falls short in providing sufficient coherent processing time due to the range migration of the target. Therefore, it serves as a starting point for the (more advanced) method in section 2.2.5.

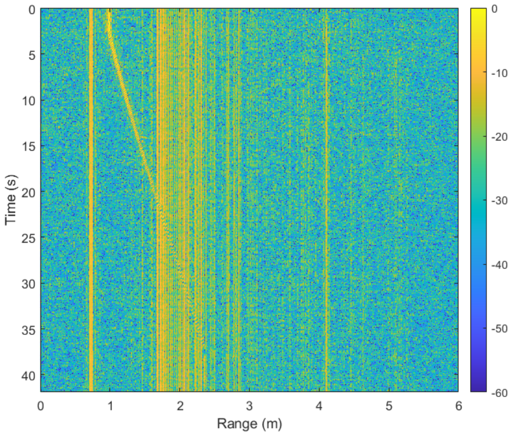

(a) Short-time matched filter

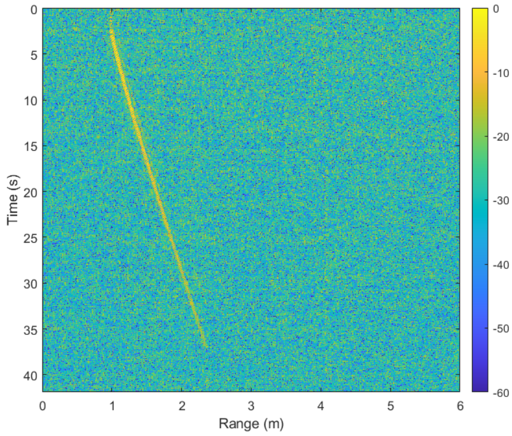

(b) Short-time matched filter using MTI filter

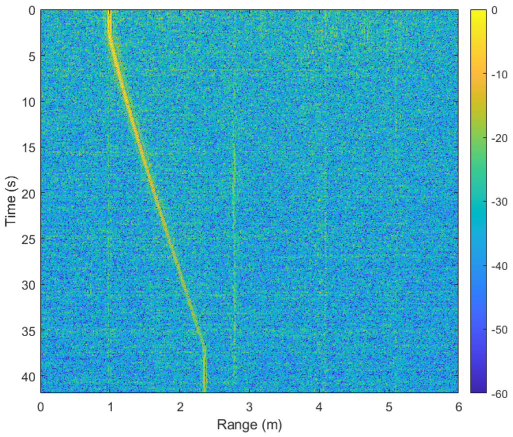

(c) Short-time matched filter using CLEAN

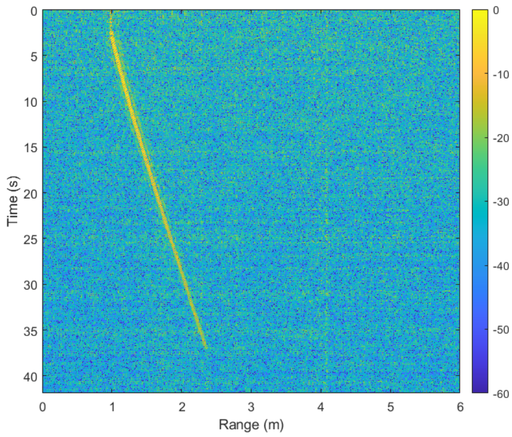

(d) Short-time matched filter using CLEAN + MTI

Figure 2.6: Range-time images using clutter filtering for a moving target experiment in the in-air demonstrator. CW PRN is as transmit waveform. Shown is the normalised output of $|s_{MF}(t',m)|^2$ in dB for segments of 4096 samples, or $T_w \approx 85$ ms. The straight lines seen in (a) are main-lobes corresponding to the clutter and are removed in (b) using an MTI filter. The sidelobes are only removed in (c) and (d) using CLEAN. The best result is obtained using CLEAN + MTI.

From Eq. 2.45 it is seen that $s_{MF}(t',m)$ is modulated by a Doppler shift over slow-time m. The frequency content, or the rate of change of this phase term, is then extracted using a Fourier transform over slow-time. That is, a Fourier transform over the columns of the range-time image (so at fixed range indices). A derivation is given below to determine the resolution that is obtained with this method. If the target is within the same range bin for multiple slow-time windows (one CPI), a Fourier transform of the signal over slow-time, is given by

$$s_{MF}(t', f) = \int \alpha e^{j2\pi f_D m T_w} \chi_{g,\mathrm{NB}}(t' - \tau(m), f_D) e^{-j2\pi f m} dm. \tag{2.50}$$

Here we assume that we can approximate $\chi_{g,\mathrm{NB}}(t' - \tau(m), f_D)$ as a rectangular window in slow-time m, centred at $m_0 = (\frac{2r_0}{c} - t') \cdot \frac{c}{2vT_w}$. The width of the window is the number of slow-time samples of the target in a range-bin: $N_m = T_{CPI}/T_w \approx \frac{\Delta R}{vT_w}$, where $T_{CPI} \approx \Delta R/v$ is the time the target spends in the range bin. This gives the following expression for the Fourier transform over slow-time:

$$\begin{aligned}
s_{MF}(t', f) &= \int_{m=m_0-\frac{T_{CPI}}{2T_w}}^{m_0+\frac{T_{CPI}}{2T_w}} \alpha e^{-j2\pi m(f - f_D T_w)} dm = \frac{j\alpha}{2\pi(f - f_D T_w)} \left[e^{-j2\pi m(f - f_D T_w)}\right]_{m_0-\frac{T_{CPI}}{2T_w}}^{m_0+\frac{T_{CPI}}{2T_w}} \qquad (2.51) \\
&= \frac{j\alpha}{2\pi(f - f_D T_w)} \left(e^{-j2\pi(m_0+\frac{T_{CPI}}{2T_w})(f - f_D T_w)} - e^{-j2\pi(m_0-\frac{T_{CPI}}{2T_w})(f - f_D T_w)}\right) \\
&= \frac{j\alpha}{2\pi(f - f_D T_w)} e^{-j2\pi m_0(f - f_D T_W)} \cdot -2j sin\left(2\pi \frac{T_{CPI}}{2T_w}(f - f_D T_w)\right) \\
&= \alpha \frac{sin\left(\pi(\frac{T_{CPI}}{T_W})(f - f_D T_w)\right)}{\pi(f - f_D T_w)} \cdot e^{-j2\pi m_0(f - f_D T_w)},
\end{aligned}$$

which is a sinc-function with a mainlobe width of $\Delta f = \frac{2T_w}{T_{CPI}}$. From this expression it is clear that the Doppler resolution increases with the coherent processing time T_{CPI}, so a wide window in slow-time leads to a narrow peak, thus a more accurate estimation of Doppler. The target frequency is estimated by the maximum of the sinc-function such that $f = f_D T_w$, where $f_D = \frac{2v}{c} f_c$. The target velocity is then found by

$$v = f \frac{c}{2f_c T_w}. \tag{2.52}$$

The resolution in velocity is then found from the mainlobe width of the frequency spectrum, which is the $\frac{2T_w}{T_{CPI}}$ width of the sinc-function:

$$\Delta v = \Delta f \cdot \frac{c}{2f_c T_w} = \frac{2T_w}{T_{CPI}} \cdot \frac{c}{2f_c T_w} = \frac{c}{f_c T_{CPI}}. \tag{2.53}$$

Interestingly, this result is the same as the expected resolution from the ambiguity function of PRN (see section 2.1.2) for a signal of length $T = T_{CPI}$.

The frequency is bounded by the Nyquist frequency, which since f is normalised by the PRF ($f = f_D T_w = f_D/PRF$), is bounded by $f_{max} = \frac{1}{2}$. Therefore, the maximum detectable velocity using this method is

$$v_{max} = f_{max} \cdot \frac{c}{2f_c T_w} = \frac{c}{4f_c T_w}. \tag{2.54}$$

In Figure 2.7, the range-time image of a simulated moving target is given in (a) and the pulse-Doppler processing method in (b). It is concluded that the traditional method of moving target detection only achieves a short coherent integration time, namely T_{CPI},

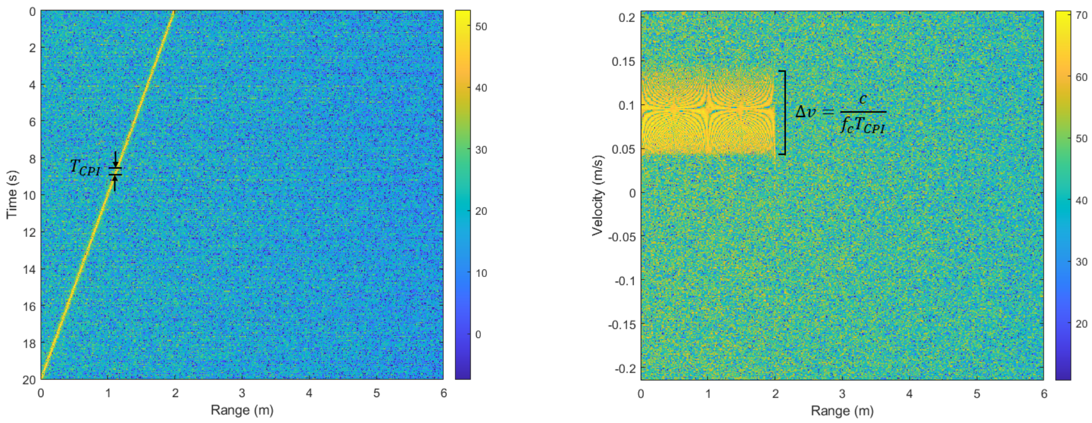

(a) Short-time matched filter in dB power

(b) Fourier transform over the columns of $s_{MF}(t', m)$ in dB power

Figure 2.7: Simulation of a moving target at $r_0 = 2$ m with constant velocity $v = 0.1$ m/s, using a CW PRN signal. Shown is the matched filter output (a) and a Fourier transform over the columns of $s_{MF}(t', m)$ (b). The resolution in Doppler is limited by the time a target is observed at a constant range.

which is limited by the range migration of the target and therefore gives insufficient gain and resolution. In order to extend the coherent integration time of a moving target, the range migration should be considered. Luckily, the coupling between the phase term and the angle of the migrating target can be used to simplify, as will be explained in the next section.

2.2.5 Coherent integration using the Radon-Fourier transform

The short-time matched filter operates on short-time intervals in which the target appears static. Aside from the simplifications caused by the assumption that $v \ll c$ and $|vT_w| \ll \Delta R$, the output of the matched filter method should contain all the information of the moving target signal. In this section, long time coherent integration of the target is therefore proposed by integrating over the output of the short-time matched filter.

The time delay of an echo from a moving target with a constant radial velocity v_T and initial range r_0, is $\tau(t) = \frac{2(r_0 - v_T t)}{c}$. This generates a straight line in range-time, under an angle that corresponds to the velocity of the target and an initial range at $t = 0$. Furthermore, the Doppler shift of the signal reflecting from a target is also dependent on its' velocity. Therefore, there is a coupling in range-time between the angle and the Doppler phase shift of the straight line, which we aim to exploit in this section. If the Fourier transform is used to extract the Doppler, as seen in the previous section, the Doppler resolution is limited by the time the target spends in one range resolution cell. However, if the integral could be applied over a line under the right angle (Radon transform), the integration time and thus resolution would increase. However, computing the Fourier transform for all angles and then detecting where it obtains a maximum, is not very efficient as it spans an extra dimension.

Rather, we can use the coupling between the Doppler induced phase-shift and the range migration to express both in terms of the velocity of the target. More specifically, the delay in slow-time is $\tau(m) = \frac{2r_0}{c} - \frac{2v_T}{c}mT_w$ and the Doppler phase shift in the output of Eq. 2.45 is given by $e^{j2\pi f_D mT_w} = e^{j2\pi\frac{2v_T}{c}f_c mT_w}$, both expressed in terms of the target speed v_T. Combining the integration over a line-segment while compensating for the phase (Fourier) term, gives the so called Radon-Fourier transform (RFT) [24]. In this thesis the RFT is written as a function of the short-time matched filter, giving

$$s_{RFT}(r, v) = \int_{mT_w=0}^{T} s_{MF}(\tau_s(m), m)e^{-j2\pi\frac{2v}{c}f_c mT_w}dm, \tag{2.55}$$

where $\tau_s(m) = \frac{2r}{c} - \frac{2v}{c}mT_w$ is the search delay, for which we use initial range r and a search velocity v for a constant velocity model. However, the search could be easily extended to include acceleration (e.g., by substituting $v' = v + a(mT_w)$). Using the expression for $s_{MF}(t', m)$, we see that the RFT method is 'matched':

$$s_{RFT}(r, v) = \int \alpha\chi_{g_m,\mathrm{NB}}(\tau_s(m) - \tau(m), \frac{2v_T}{c}f_c)e^{j2\pi\frac{2v_T}{c}f_c mT_w}e^{-j2\pi\frac{2v}{c}f_c mT_w}dm, \tag{2.56}$$

as the peak amplitude in $s_{RFT}(r, v)$ will be observed at initial range $r = r_0$ and $v = v_T$, which maximises the ambiguity function for $\tau_s(m) = \tau(m)$ and cancels the complex exponential. As seen from Eq. 2.56, the amplitude of the RFT peak is given by integrating the short-time ambiguity functions over m, evaluated at their peaks: $|\chi_{g_m,\mathrm{NB}}(0, \frac{2v}{c}f_c)|$. The amplitude of the peak of the RFT method will then be: $|s_{RFT}(r_0, v_T)| = |\Sigma_m(\chi_{g_m,\mathrm{NB}}(0, \frac{2v_T}{c}f_c))|$. Comparing this to $|\Sigma_m(\chi_{g_m,\mathrm{NB}}(0, 0))|$, gives the loss due to the assumption that Doppler is negligible within one segment.

Figure 2.8 shows the result of the RFT for a moving target simulation using CW PRN for an in-air scenario. The peak corresponds to the moving target as detected by the Radon-Fourier transform of the short-time matched filter output. The RFT result reveals it's the similarity with the ambiguity function of the transmit signal, but then centred at a non-zero initial range and velocity. The ambiguity function essentially describes the matched filter response to a Doppler shifted echo, therefore, the RFT can be seen as an extension of a matched filter for multiple pulses.

The most notable sidelobe pattern observed in the RFT in Figure 2.8 are two line crossing the peak. These can be attributed to partial correlations of the moving target signal with the signal produced by a different trajectory that overlap at a certain point. For example, integration in range-time from the correct initial range but with an incorrect velocity, produces a vertical sidelobe line, as seen in the RFT. In Figure 2.8, the RFT is also compared to a Radon transform on the absolute value of the output of the short-time matched filter, which neglects the phase content. What is seen is that the RFT obtains the peak-to-sidelobe ratio of coherent integration, whereas the Radon transform achieves only half the peak-to-sidelobe ratio (in dB power).

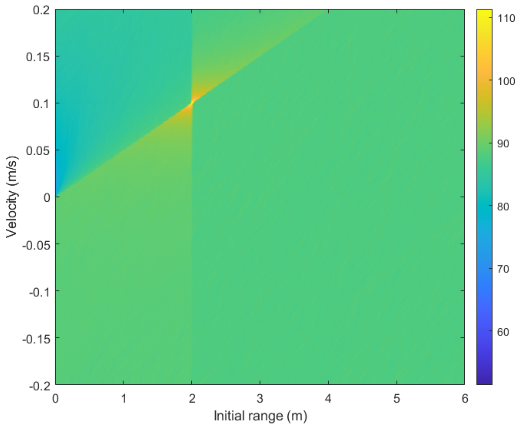

(a) Radon transform of $|s_{MF}(t', m)|$ in dB power for a simulated moving target

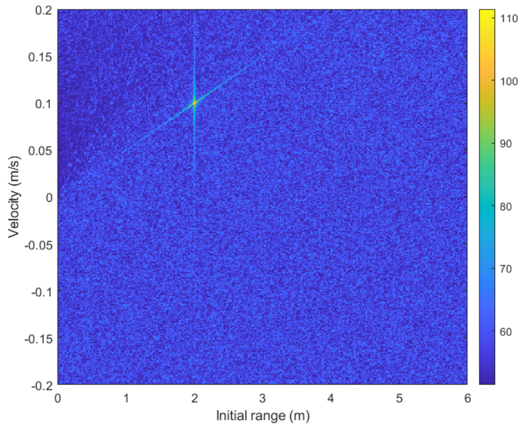

(b) Radon-Fourier transform of $s_{MF}(t', m)$ in dB power

Figure 2.8: Radon transforms on a simulated range-walk with an initial range $r_0 = 2$ meter and target velocity $v_T = 0.1$ m/s. Both the Radon transform of $|s_{MF}(t', m)|$ and the RFT show a peak of 111.4 dB. Compared to an exact matched filter, which achieves $20log_{10}(\boldsymbol{s}^H\boldsymbol{s}) =$ 112.1 dB, the loss is limited to 0.7 dB in power. The background of the RFT is lower, at approximately 50 dB below peak, than the background of the Radon transform of $s_{MF}(t', m)$, which is approximately 25 dB below peak.

2.3 Results

In this section, the proposed (RFT-based) method for coherent integration is verified and compared to a matched filter bank for moving targets in section 2.3.1. Then, after having established that the RFT method gives the desired output, the method is used to compare the imaging performance for a simulated moving target using PRN and HFM pulses. Lastly, the results of the in-air measurements of a moving target using the proposed waveforms are given in section 2.3.2.

2.3.1 Simulations

Comparison with a matched filter bank

To test the RFT-based method, the signal of a moving target is simulated for a harbour scenario ($c = 1500$ m/s). The signal is generated by interpolating the digital transmission, which is a real-valued bandpass signal, with a set of indices that correspond to the delay $\tau(t)$ of the target. The matched filter bank, which we compare the proposed method against, is computed in the same way, but then for a wide range of velocities.

The proposed method using the RFT is implemented first without the clutter filter, since the simulated received signal is clutter-free. Here the simulated target has an initial range $r_0 = 10$ m, with a velocity $v = 0.2$ m/s. The transmit signal is chosen to be a 20 seconds CW PRN signal, with $f_c = 12.5$ kHz and a bandwidth $B = 5$ kHz, over-sampled at a rate of $F_s = 100$ kHz. The range-time window length are chosen

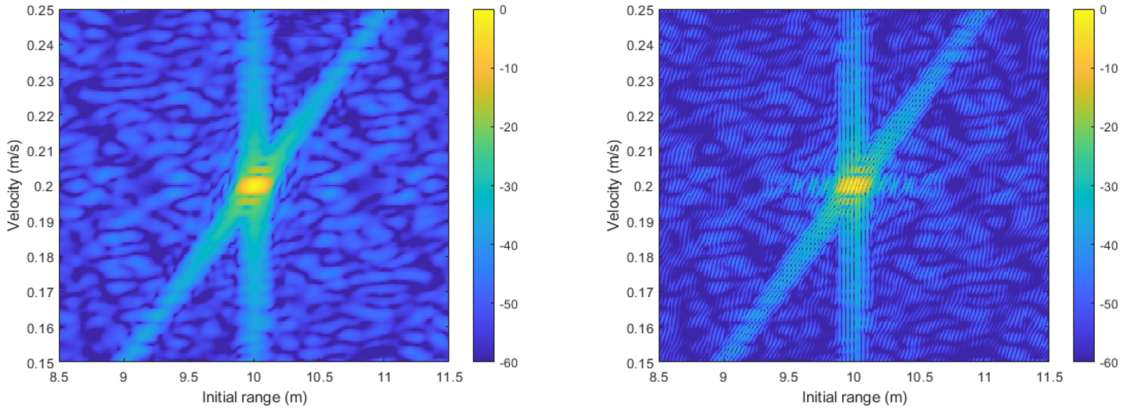

(a) RFT

(b) Matched filter bank

Figure 2.9: A comparison of the (zoomed in) output of the matched filter bank and the proposed method (RFT), for a simulated moving target. An approximate peak-to-sidelobe ratio of $10log_{10}(5 \cdot 10^5 \cdot 20) = 50$ dB is observed, as expected from coherent integration. An almost identical pattern is observed for the RFT and the MF bank, the difference being that for the RFT the envelope of the MF bank output is observed.

to be $L_w = 1024$ samples, corresponding to $T_w \approx 10$ ms. In this case the condition $|vT_w| << \Delta R$ is satisfied by $1 << 75$.

Figure 2.9 show the output of the matched filter bank and of the proposed method. It shows that both give almost identical output, which was expected. The main difference is that the RFT uses the baseband signal, whereas the matched filter bank here operates on the bandpass signals. The effect can be seen in the zoomed plots on the right, as the modulation of the carrier is visible for the MF bank, whereas for the RFT the envelope is visible.

Comparison of waveforms

To see which pulse type has better sidelobes in the initial range-velocity domain, the RFT method is applied to pulsed PRN and HFM. First, a close-by target (harbour scenario) at an initial range of 10 meters is considered, the same as in Figure 2.9. A PRI of 100 ms and a pulse duration of 10 ms is chosen. This gives a maximum detection range of $R_{max} = PRI \cdot c/2 = 75$ m. As noted before, $T_w = 10$ ms is a short enough window size such that $|vT_w| \ll \Delta R$, we can therefore apply the short-time matched filter per PRI. The simulation results of pulsed PRN and HFM are shown in Figure 2.10. The main difference that is observed is that the sidelobe level in both range-time and initial range-velocity is better for HFM.

When the target is far out, the echo can take much longer to return and so the PRI and pulse duration will be increased. Here an example is considered where the $PRI = 1$ s and the pulse duration is 0.2 s, corresponding to a detection range of min 150 m and max 750 m. Using these parameters, a target is simulated, moving from 500 m with a constant radial velocity of $v = 0.5$ m/s. Now the PRI is too long to neglect Doppler

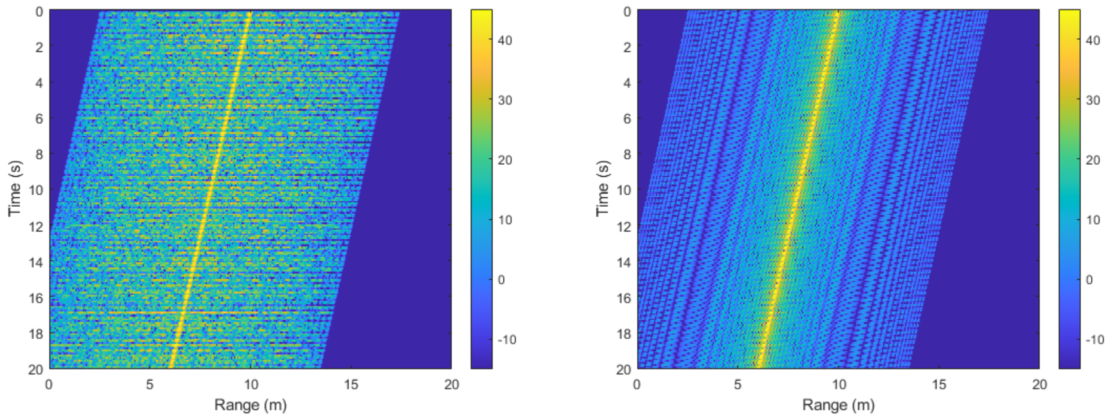

(a) Short-time matched filter for PRN pulses (b) Short-time matched filter for HFM pulses

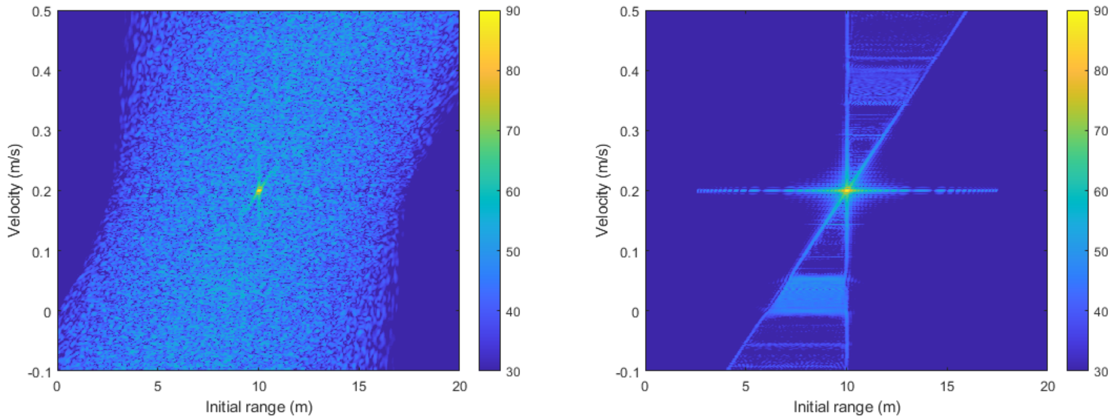

(c) RFT for PRN pulses (d) RFT for HFM pulses

Figure 2.10: Comparison of the performance of PRN and HFM in a noise- and interference-free harbour scenario for a close-by moving target. The PRI is 0.1 s with a pulse duration of 10 ms (200 short pulses). The matched filter response per pulse are stacked to get range-time, as seen in (a) and (b). The sidelobes of the target are limited in range, since the pulse ends within the correlation window ($R_{sl} = \pm cT_{pulse}/2 = \pm 7.5$ m from the position of the target). Sidelobe levels in range-time are lower for HFM, as expected from the ambiguity function of the waveforms.

during one PRI. We could again split up the signal into short enough segments (which would now be shorter than one pulse duration) and apply the short-time matched filter. Integrating over the sub-pulses then again leads to coherent integration of the target signal. However, now we consider the effect of applying a short-time matched filter over the whole PRI, where the Doppler is non-negligible over the pulse duration. Hopefully, we can use the Doppler tolerant property of the HFM pulses to maintain the gain of the matched filter. The advantage would be that we have less samples in slow-time, which speeds up the RFT method for HFM and achieves the same processing gain.

Simulation results are shown in Figure 2.11 for both pulsed PRN and HFM pulses.

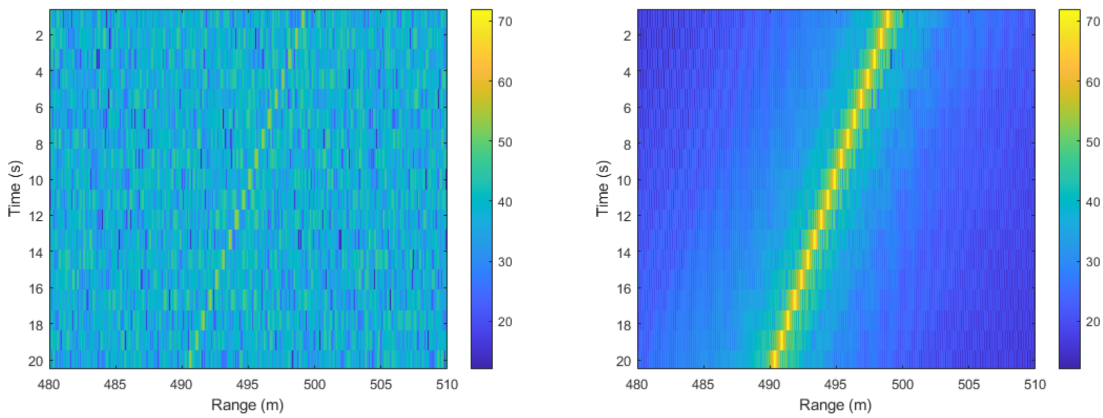

(a) Pulsed PRN

(b) HFM pulses

Figure 2.11: Comparison of the performance of PRN and HFM for a simulated far-out target, with a PRI of 1 s and pulse duration of 0.2 s (20 long pulses). Here the pulse duration is such that the Doppler is no longer negligible. A loss of about 20 dB in power for the pulsed PRN signal is observed, while the correlation gain for a HFM pulse is preserved. A translation in range ($\Delta\hat{r}_0 \approx 0.2$ m) is observed for the same target position using HFM compared to PRN pulses.

What is seen is that for a constant velocity moving target, the correlation gain of the PRN pulse deteriorates if we process the signal over the whole PRI, while the HFM pulse maintains correlation gain. This is expected from the ambiguity functions of the two signals, where the MF response of a HFM pulse will simply translate in range in the presence of uncompensated Doppler. After having detected the velocity of the target in the RFT, the shift in initial range can be predicted from the ambiguity function of a single pulse, thus being easily compensated. So, the Doppler tolerant property of the HFM can be exploited to speed up the RFT-method, because a sub-PRI segmentation of the signal is not required for this waveform, as long as the target can be assumed to have a constant velocity over the pulse duration.

2.3.2 In-air measurements

To verify the methods and simulations, a moving target experiment is performed in the in-air demonstrator. A schematic of the setup can be seen in Figure 2.1. A bulb is hoisted up towards the ceiling of the room, using a thin wire connected to the shaft of an electric drill, to emulate a moving target. The object is hoisted up in between the tweeter and microphone, which are on the ceiling of the room, while the tweeter transmits various acoustic signals. The analog microphone and tweeter are connected to an audio interface placed outside the room, as seen in Figure 2.12. The transmit signals have a bandwidth $B = 8$ kHz at a centre frequency of $f_c = 8$ kHz. The tweeter is placed at about 25 cm from the microphone, and so the direct path is the main source of interference during these measurements. The strongest noise source during these measurements was the electric drill, as seen in the sample recording shown in

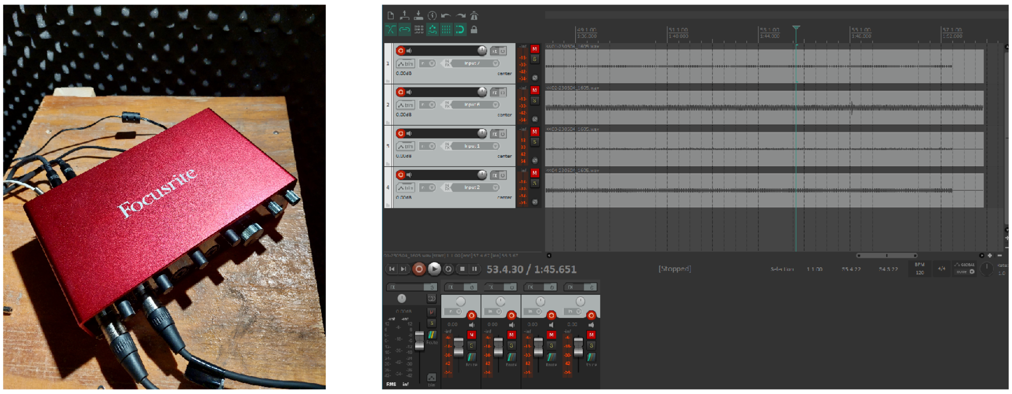

Figure 2.12: Audio interface (Focusrite 18i8) used to make the measurements (shown on the left). Two microphones (Superlux ECM999) are connected through the XLR cables on the front of the interface. On the back are three line inputs, one for the encoder and two for the analog transmit signal. The interface is connected to a laptop through USB, from which the transmit signal is played. On the right the used recording software (Reaper) is displayed, from which the four channels are synchronously recorded. Recordings are exported to WAV files and then processed using MATLAB.

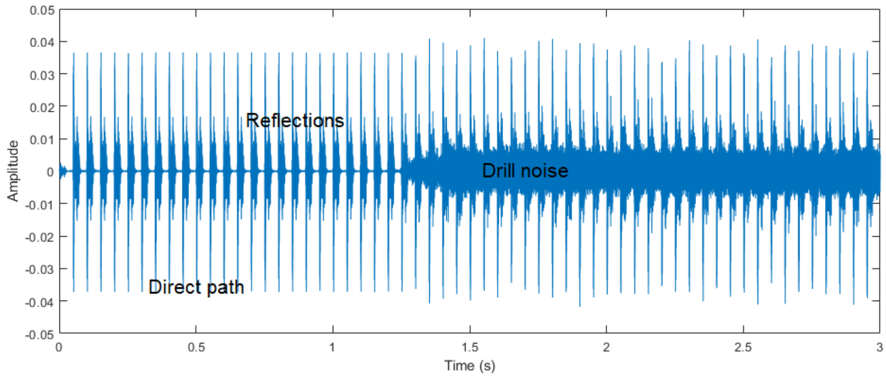

Figure 2.13: A section of an in-air moving target measurement (bandpass filtered) using HFM pulses. Here the $PRI = 50$ ms and the pulse duration is 5 ms. The direct path interference from the transmitter to receiver has the largest amplitude. The reflections are received after the direct path peak and consist of static reflections from the room and the target. The drill noise is introduced at around 1.3 seconds and has a similar signal power to the reflections.

Figure 2.13. In total, three different waveforms were tested: CW PRN, pulsed PRN and pulsed HFM. For the pulsed signals a pulse repetition interval of $PRI = 50$ ms, and a pulse duration of $T_p = 5$ ms are chosen, which accommodate an unambiguous detection range of $R_{min} = 0.86$ m, $R_{max} = 8.56$ m.

The proposed method for coherent integration is applied to obtain a range-time and initial range-velocity image of the moving target. In these measurements, the clutter signals were removed using a combination of CLEAN and MTI filtering. The

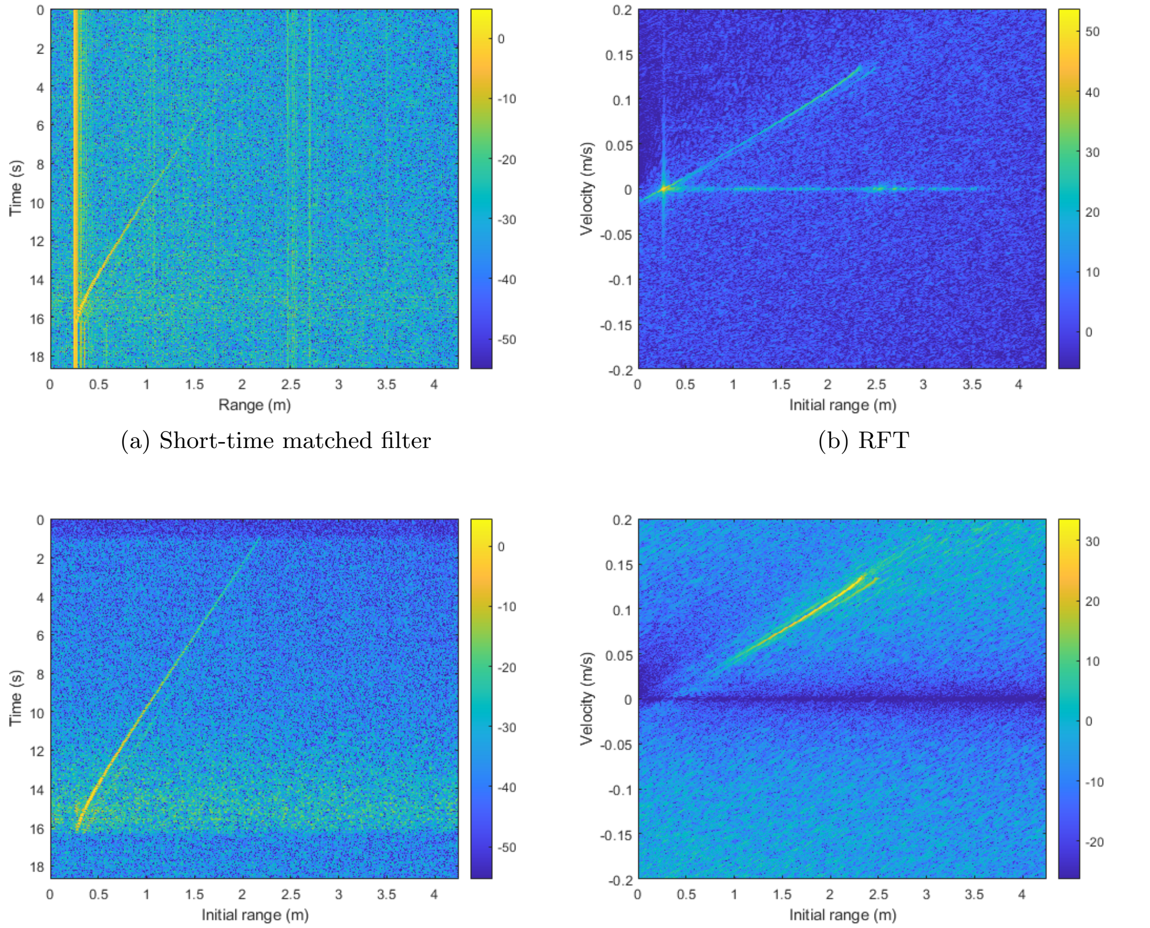

(a) Short-time matched filter (b) RFT

(c) Short-time matched filter (CLEAN + MTI) (d) RFT (CLEAN + MTI)

Figure 2.14: Results for CW PRN measurements. (a) shows the output of the short-time matched filter and (b) the corresponding RFT. Noticeable is the direct path interference, which is the strongest component in (a) and (b). Furthermore, the effect on a non-constant radial velocity is significant since the moving target was relatively close to the baseline of the transmit-receive pair. The effect in the RFT is that the velocity migrates towards a lower velocity as the target comes towards the middle of the transmit-receive pair. In (c) the CLEAN + MTI procedure is applied, filtering out the peak + sidelobe interference of the clutter. The remaining sidelobes are seen to originate from the target, because they grow with the target signal.

results for CW PRN are shown in Figure 2.14 and the results for pulsed PRN and HFM are shown in Figure 2.15 and Figure 2.16, respectively. Here the power of the filter outputs, without normalisation, is shown: $10log_{10}(|s_{MF}(t', m)|^2)$ for range-time and $10log_{10}(|s_{RFT}(r, v)|^2)$ for initial range-velocity. The outputs for CW PRN are 20 dB higher than that of the pulsed PRN and HFM, which is expected due to the 10% duty cycle of the pulsed signals, giving a 10 dB loss in amplitude (thus 20 dB in power) of the filter outputs. Comparing the PRN and HFM pulses, it is seen that the HFM

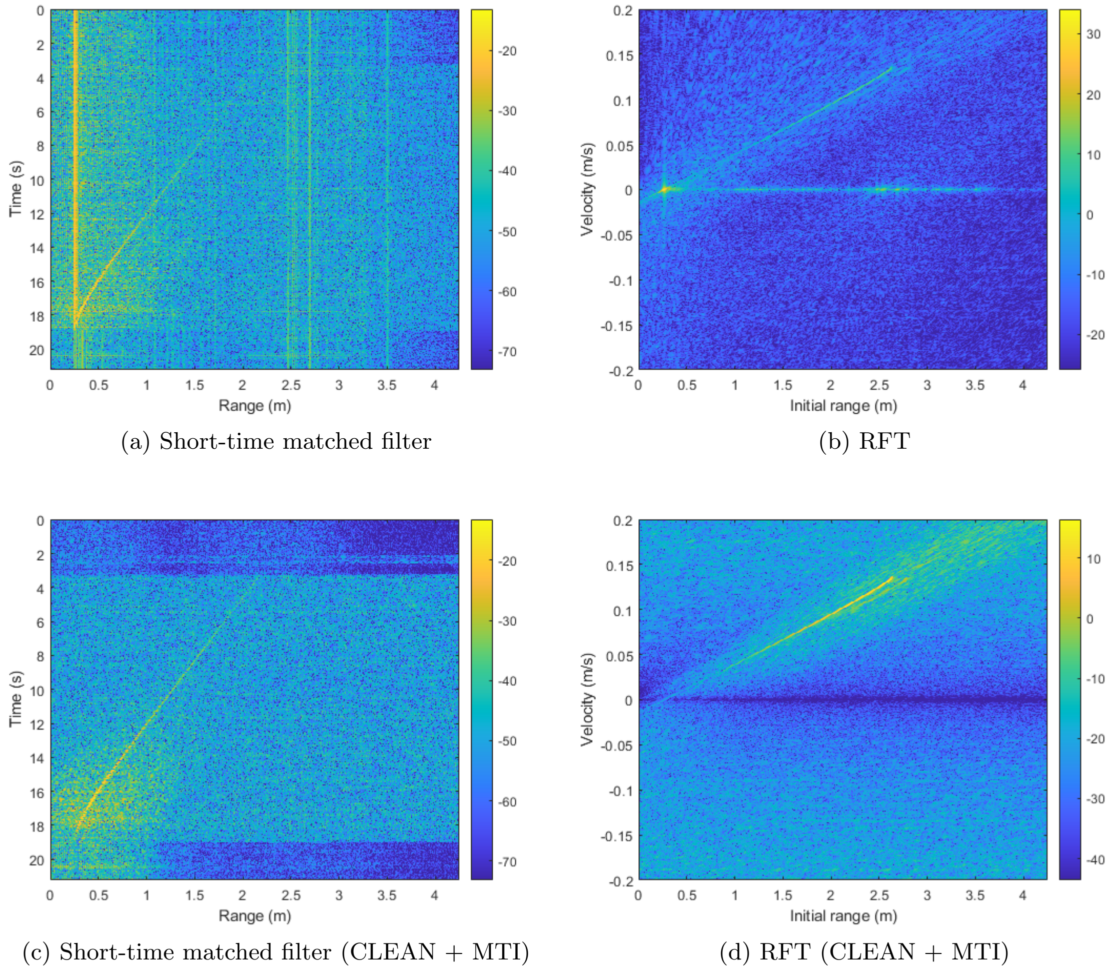

(a) Short-time matched filter

(b) RFT

(c) Short-time matched filter (CLEAN + MTI)

(d) RFT (CLEAN + MTI)

Figure 2.15: Results for pulsed PRN measurements. In the short-time matched filter, each row corresponds to one pulse. The effect of introducing silence gaps in the transmission is seen, if we compare the results against the CW PRN results in Figure 2.14. Sidelobe interference is not spread out over the entire image, but only proportional to to the pulse duration, as seen in Figure (c). Now the effect of noise and sidelobes can also be distinguished, for example the noise band stretching from $T = 3$ to $T = 18$ s, due to the noise of the drill.

pulses have a better peak to sidelobe performance in both the range-time and initial range-velocity domain. Furthermore, clutter suppression is easier for repetitive pulses (HFM), using MTI, than for non-repetitive pulses (PRN), which required first CLEAN and then MTI. Noticeably, the integration gain using the RFT method is not as high as the simulations for a constant-velocity target. This is caused by the migration of the target in initial range-velocity, which is observed from the RFT results. This migration is caused by separation of the receiver and transmitter (0.25 m), which is relatively large compared to the distance of the target and sensors (2 m to 0.25 m). This introduces an acceleration component in the two-way range to the target, which limits the processing gain of the RFT.

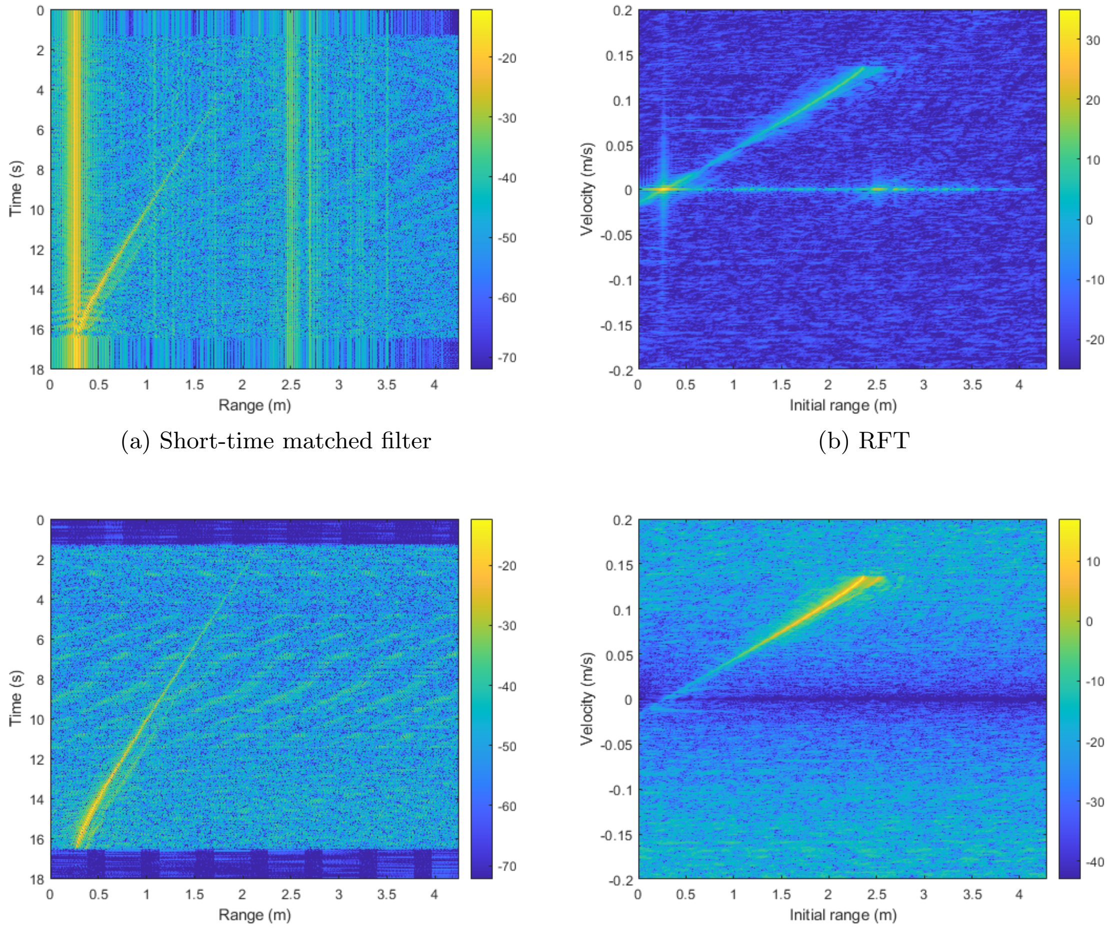

(a) Short-time matched filter

(b) RFT

(c) Short-time matched filter (MTI)

(d) RFT (MTI)

Figure 2.16: Results for HFM measurement. In (a) the effect of the drill noise is seen in between $T = 2$ and $T = 16$ s. Outside this band we see that there is little noise and the clutter components can be separated, due to the low sidelobe level of the HFM pulse (again one row corresponds to one pulse). The coherent integration of the large number of HFM pulses (≈ 300 pulses) is seen to unambiguously reveal the target velocity and initial range in (d), with a wider mainlobe but lower sidelobe level than that for pulsed PRN.

2.4 Discussion and Conclusion

In this chapter, an answer is provided to the question posed in the start of this chapter: "*How to apply coherent integration over multiple pulses for moving target detection?*".

The answer is given as a proposed processing method, which requires a model of the target's motion. A constant velocity model is adopted in this chapter, but more complicated models could be considered in the future. In the proposed method, the short-time correlations of the transmit signal with the echo are extracted using the 'short-time matched filter'. Secondly, the clutter interference is filtered out, ideally only leaving the correlations corresponding to the moving target. Coherent integration is then achieved using the Radon-Fourier transform (RFT), which is shown to provide an estimate of the initial-range and velocity of the target over the integration interval. The method is shown to be equivalent to a matched filter bank for (clutter-free) moving targets, but achieves coherent integration more efficiently. The actual detection of the moving target is not covered in this chapter, but can be implemented by setting an appropriate threshold on the output of the proposed method.

Whether a realistic moving target can be accurately modelled by having a constant velocity remains a question, and will be highly dependent on the moving target. If the target is deviating from a constant velocity over the period of integration, the integration gain will be decreased. Therefore, it is important to find a suitable integration time, which is not investigated in this thesis. Furthermore, the integration losses that occur are increased if the range resolution and velocity resolution of the system are increased. As seen in this chapter, the resolution in range and velocity improves with bandwidth and carrier frequency, respectively. Therefore, limiting the carrier frequency and bandwidth could make the system more robust against integration losses for non-ideal moving targets. However, modifying these parameters has a direct impact on the SNR, as illustrated by the sonar equation in section 1.2.1. This makes it challenging to find the optimal system parameters without prior knowledge of the moving target. A final aspect that is considered regarding the constant velocity assumption, is the effect of the target angle, i.e., if the target is moving radially towards to the sonar or under an angle. From the analysis provided in section 2.4, it is concluded that the target angle is not expected to have a significant effect on the constant velocity assumption for the considered ranges.

In attempt to answer the other question posed in this chapter: "*What is the optimal transmit waveform for detecting a moving target in a clutter dominated environment?*", two waveforms have been proposed: pseudo-random noise (PRN) and chirps (HFM). If the integration interval is limited to only a single pulse, then PRN appears to be a good candidate, since it can unambiguously resolve a target in range and Doppler. However, as shown in this thesis, HFM can also be used to resolve the target unambiguously using coherent integration over multiple pulses. Under the condition that multiple pulses can be integrated, it is concluded that HFM pulses perform better than PRN pulses. This is concluded from the results obtained from simulations and in-air measurements, based on the following three reasons:

1. The sidelobe performance for HFM pulses is superior to that of PRN pulses.
2. Clutter is removed more efficiently using HFM pulses, i.e., using an MTI filter.
3. The processing is simplified with HFM pulses due to their Doppler tolerant property.

However, as demonstrated in this thesis, using CW transmit signal such as CW PRN could result in a higher processing gain. Therefore, the question remains whether a pulsed or CW transmit signal is better for detecting a moving target. The answer is that it will depend on the clutter interference and the extend to which it can be

	$r_0 = 100$ m	$r_0 = 250$ m	$r_0 = 500$ m	$r_0 = 1000$ m	$r_0 = 2000$ m
$v_T = 0.25$ m/s	23.7 s	38.0 s	54.0 s	76.7 s	108.8 s
$v_T = 0.5$ m/s	11.9 s	19.0 s	27.0 s	38.3 s	54.4 s
$v_T = 1.0$ m/s	5.9 s	9.5 s	13.5 s	19.2 s	27.2 s

Table 2.1: Integration time in seconds from which the velocity error will exceed the velocity resolution. Results are shown for a target moving at various speeds and initial ranges at an angle of $\theta = 45\,\text{deg}$.

cancelled in a realistic scenario. Namely, any uncompensated clutter interference will produce sidelobes over the whole imaging range. In section 2.4, estimates are provided for the remaining clutter interference that is 'allowed' for CW PRN in order to detect a moving target. A similar analysis could be done for CW HFM signals, but is not provided here. The conclusion drawn from this analysis is that in a practical long-range detection scenario, it is unlikely that a CW transmission can be used.

Considering the effect of the target angle

The angle of the moving target with respect to the transmitter and receiver will have an effect on the measured radial velocity. For non-radial motion, an acceleration component is introduced as seen in the in-air measurements. This will limit the duration over which we can assume the target has a constant radial velocity and thus the integration gain if we process for only constant velocities. However, this effect diminishes as $R \gg v_T T_{int}$, for an integration time T_{int}, and will be well approximated by $v_r \approx v_T cos(\theta)$, where θ is the off-radial angle to the sensors. The following analysis provides insight in the ranges and target velocities for which the target angle can be neglected.

Consider the path of a target moving at a constant velocity, in the xy-plane as:

$$x(t) = x_0 + v_x t = x_0 + sin(\theta) v_T t, \quad y(t) = y_0 - v_y t = y_0 - cos(\theta) v_T t, \tag{2.57}$$

where the radius to a target with initial coordinates (x_0, y_0) at a fixed angle θ can then be expressed as

$$r(t) = \sqrt{x^2(t) + y^2(t)} = \sqrt{(x_0^2 + y_0^2) + (v_T t)^2 + (2x_0 sin(\theta) - 2y_0 cos(\theta)) v_T t}. \tag{2.58}$$

The true radial velocity defined towards the sensors at $(0,0)$ is

$$v_r(t) = -\frac{dr(t)}{dt} = -\frac{v_T^2 t + (x_0 sin(\theta) - y_0 cos(\theta)) v_T}{\sqrt{(v_T t)^2 + (2x_0 sin(\theta) - 2y_0 cos(\theta)) v_T t + (x_0^2 + y_0^2)}} \tag{2.59}$$

To determine how large the error is in assuming a constant radial velocity over a certain time interval, the error made by assuming $v_r = cos(\theta) v_T$ is compared against the velocity resolution that would be achieved by coherent integration over the interval.

The following parameters were assumed for a realistic target speed and distance in a harbour scenario: $c = 1500$ m/s, $f_c = 8$ kHz, and a target angle of $\theta = 45\,\text{deg}$.

Using the result that the expected resolution in velocity is $\Delta v = \frac{c}{f_c T_{int}}$, we can find the integration time $t = T_{int}$ for which the velocity error $v_e(t) = |v_T cos(\theta) - v_r(t)|$ equals the velocity resolution. In table 2.1 the results of a numerical analysis on the maximum integration time are shown. It is seen that the maximum integration time roughly halves for doubling the speed of the target and that the error has less effect the larger the range is. It is concluded that the constant velocity approximation can be used for at least up to $T_{int} = 10$ seconds, for velocities up to 1 m/s, as the error made by the approximation is then within the velocity resolution. At all angles $|\theta| \leq 45\,\text{deg}$ the velocity error is even less, so similar to better integration times should be achievable for a constant velocity target. The main takeaway of this analysis is that the target angle can be neglected for a low-speed target at large range. The actual manoeuvring, e.g., an acceleration or change of direction of the target, is expected to have more impact on the constant velocity assumption.

Conditions for CW PRN

If the integrated signal of the moving target is stronger than the sidelobes of remaining clutter, then a CW transmit signal has an advantage because of the additional noise suppression. In section 2.2.3 the conditions for detection of a moving target using CW PRN are given. This is important if clutter signal remains after having applied a clutter filter (CLEAN + MTI in the case of CW PRN), which is expected in a realistic scenario due to non-static clutter signals, e.g., from reflections of the sea surface. Currently, CLEAN and MTI filtering are proposed, but can only handle purely static clutter. Therefore, more sophisticated clutter filters could be designed that can, for example, track the slowly moving clutter signal in range-time to accurately remove it.

In order to make some simple estimates, the condition for a CW transmit signal (Eq. 2.46) is rewritten in terms of relative target strength and range, assuming spherical spreading (power drops as $\propto 1/R^4$) of the two-way signal. Here the relative target strength is defined as $TS_r = TS_{target}/TS_{clutter}$, such that the clutter to target power can be written as $\frac{P_{target}}{P_{clutter}} = (\frac{R_{target}}{R_{clutter}})^4 \frac{1}{TS_r}$. Substituting this in Eq 2.46 gives the following condition in terms of decibels:

$$10log_{10}(BT_{int}) > 40log_{10}(R_{target}/R_{clutter}) - 10log_{10}(TS_r). \tag{2.60}$$

Using this expression, the required integration time for CW PRN is given in Figure 2.17 for a bandwidth of 5 kHz. The target strength TS of the strongest clutter component is assumed to be at least as strong as the TS of the moving target. This figure shows that if there is remaining clutter interference at, for example, 1/10th the range of the moving target, that an integration time of 1 to 10 seconds will be enough for an optimistic relative target strength in between 0 dB and -10 dB. However, if the distance is at 1/20th to 1/30th of the target, then is unlikely that the integration time can be achieved for any reasonable TS_r. For detection on a kilometer range, an uncompensated clutter component at a range of more than 100 m, will likely mask the moving target, therefore prohibiting the use of CW PRN.

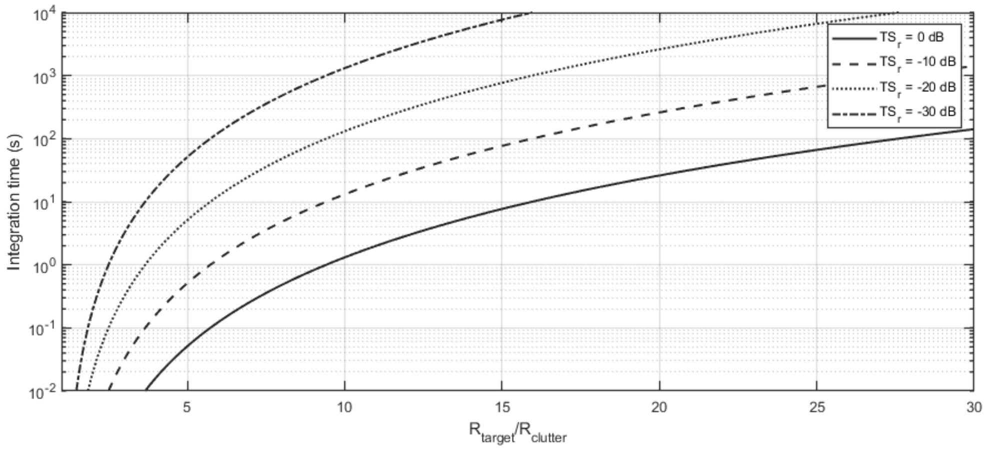

Figure 2.17: Integration time in seconds for CW PRN with $B = 5$ kHz, at which the clutter sidelobe level equals the integrated target level. The integration time is given as a function of relative target strength and relative range of the target and clutter.

Note that in Figure 2.17, the integration time for which the average sidelobe level of a PRN clutter signal equals the moving target level. To make a working detector, the target signal should be above the interference level, thus a higher integration time is actually needed than that given in the figure. In conclusion, it is expected that in practical scenarios where clutter interference cannot be completely mitigated, it is essential to include periods of silence in the transmit signal.

3 Synthetic aperture imaging

In this chapter, coherent integration is applied to synthetic aperture imaging with the aim to improve the imaging capabilities under low SNR conditions. The use of low-to-medium frequencies and a high positioning accuracy of the sensors is considered for coherent integration over the sensor trajectory. This overcomes some of the limitations of existing SAS systems, which require a minimum echo strength of a single pulse. Similar to the previous chapter, the application of high duty-cycle or CW transmit signals such as PRN is explored in this chapter to maximise the SNR gain.

In contrast to the previous chapter, the sonar sensors (transmitter and receiver) are now in motion and the imaging scene is static. From the motion of the sensor a 'synthetic aperture' is created, which means that the echoes received from multiple sensor positions are combined to form an image of a specific point in the scene. The sensor position is assumed to be known accurately over time within a small fraction of the wavelength[1]. Again, imaging from a single sensor is considered, which could be used as the basis for a low-to-medium frequency imaging system that uses an array of sensors. This leads to the formulation of the following two questions:

1. *How to process the received echoes in order to achieve coherent integration from a moving sensor pair?*

2. *What are the key parameters that influence the imaging resolution, and how can it be improved?*

The first question is discussed in section 3.1, where a signal model is provided for the echo of a static point reflector, as measured from a moving transmitter and receiver. Using the signal model, a matched filter is proposed to produce an image from the received echoes. To address the second question, the point-spread-function (PSF) is analysed and a geometrical interpretation is provided to gain insight into the parameters that influence the imaging resolution, such as the movement of the moving receiver and transmitter with respect to the scene. Then in section 3.2, the imaging model is treated as a linear system of equations. By incorporating a model for the PSF, an attempt is made to improve the imaging resolution through the application of inversion techniques. In section 3.3 the proposed processing techniques are compared in terms of imaging resolution based on simulations. Furthermore, the imaging performance is compared again for PRN and chirps (HFM), similar to chapter 2. Finally, the imaging methods are applied to real data, which is measured using a similar in-air demonstrator as for moving target detection (see Figure 3.1).

[1]Here the wavelength refers to the centre frequency $\lambda = \frac{c}{f_c}$. However, since the signals being considered are wideband, it is important to consider the wavelength of the highest frequency component to maintain coherence across all frequencies in the signal.

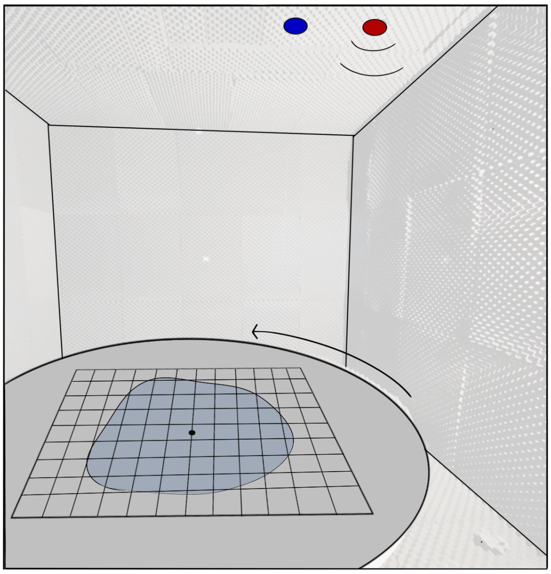

Figure 3.1: Schematic of the in-air demonstrator for synthetic aperture imaging. Similar to the setup for moving target detection, there is a separate transmitter (red) and receiver (blue) placed on the ceiling of the anechoic room. The scene that is imaged is depicted by the blue object, which is imaged on the discretized grid, after having completed one full rotation of the table on which it lies. The rotating table should emulate the relative motion for a synthetic aperture, in which the sensors themselves move.

3.1 Coherent integration for synthetic aperture imaging

In this section, a processing method for synthetic aperture imaging from a single sensor is described. The main assumption is that the position of the sensor is accurately known over time, which is used to estimate the signal delay to each point in the imaging domain, as described in section 3.1.1. A commonly made approximation for delay estimation is discussed, but the 'full solution' is provided as well, to show that the delay estimation problem is non-trivial. Using the signal delays to a point reflector over a given trajectory of the sensors, a matched filter for imaging is described in 3.1.2. The PSF resulting from a circular trajectory of the sensors is described in section 3.1.3. There, an intuitive explanation of the PSF is provided, based on the geometry of the trajectory with respect to the point reflector. This gives an approximation for the imaging resolution that is obtained. Furthermore, more complicated scenarios are investigated using simulations for various reflector positions. Finally, the imaging resolution is examined for various sensor placements, leading to some suggestions on how to maximise the imaging resolution.

3.1.1 Time delay estimation

This section described the problem of estimating the time delay of a sonar echo from a static reflector, considering that the pulse is send and received from a moving platform. For simplicity, below the transmitter and receiver are assumed to be co-located in the first steps. Later in this section, it is explained how to extend the model for the scenario where the transmitter and receiver are spatially separated.

First, consider a static sonar sensor at position $\boldsymbol{p}_s = (x_s, y_s, z_s)$ and a reflector at $\boldsymbol{p}_r = (x_r, y_r, z_r)$ as seen in Figure 3.2. If the sensor transmits a pulse, the delay of the echo is constant over time and is determined by the propagation distance between the sensor and the reflector:

$$\tau = \frac{2}{c}||\boldsymbol{p}_s - \boldsymbol{p}_r||, \tag{3.1}$$

where c is the medium velocity of sound, which is assumed to be constant. The corresponding delay can be found from the received echo, by applying pulse compression. Having estimated the delay, the point reflector is known to be located somewhere on the surface of a sphere surrounding the sensor, as seen in Figure 3.2 (a), whose radius is given by $r = \frac{\tau c}{2}$. The shell thickness of this sphere is determined by the width of the mainlobe of the pulse-compressed signal, as described in section 1.2.2.

Now consider that the sensor is not static, but moving continuously from position $\boldsymbol{p}_A$ at $t = t_A$ to $\boldsymbol{p}_B$ at $t = t_B$, as seen in Figure 3.2 (b). At $\boldsymbol{p}_A$, the sensor transmits a short pulse, which reflects from the point reflector when the sensor is at $\boldsymbol{p}_C$ and reaches the sensor again at $\boldsymbol{p}_B$. The total delay of the echo is then given by the time from transmitter to reflector plus the time back to the receiver, as

$$\tau = t_{AC} + t_{CB}. \tag{3.2}$$

Knowing the position at which the pulse is transmitted ($\boldsymbol{p}_A$), the time it takes the signal to reach the reflector at $\boldsymbol{p}_C$ is given by

$$t_{AC} = \frac{1}{c}||\boldsymbol{p}_A - \boldsymbol{p}_r||, \tag{3.3}$$

where $\boldsymbol{p}_C$ is found by $\boldsymbol{p}_C = \boldsymbol{p}_s(t_C)$, with $t_C = t_A + t_{AC}$. $\boldsymbol{p}_C$ is also known as the phase centre of $\boldsymbol{p}_A$ and $\boldsymbol{p}_B$, which is a widely used in SAS processing to simplify the processing using the Phase Centre Approximation (PCA) [6]. In the PCA, the two-way propagation distance is approximated as $||\boldsymbol{p}_A - \boldsymbol{p}_r|| + ||\boldsymbol{p}_r - \boldsymbol{p}_B|| \approx 2||\boldsymbol{p}_C - \boldsymbol{p}_r||$. The delay of the echo using the PCA is then given by

$$\tau_{PCA} = \frac{2}{c}||\boldsymbol{p}_C - \boldsymbol{p}_r||. \tag{3.4}$$

The PCA provides a good trade-off between computational complexity and image quality for short-range imaging systems if the phase errors are relatively small. The assumption made in the PCA is that the sensors follow a straight line. However, for long-range imaging the delay of an echo can be much larger. The position of the sensor can deviate significantly from a straight line, since it might follow any arbitrary path, and therefore increases the phase error made by the PCA.

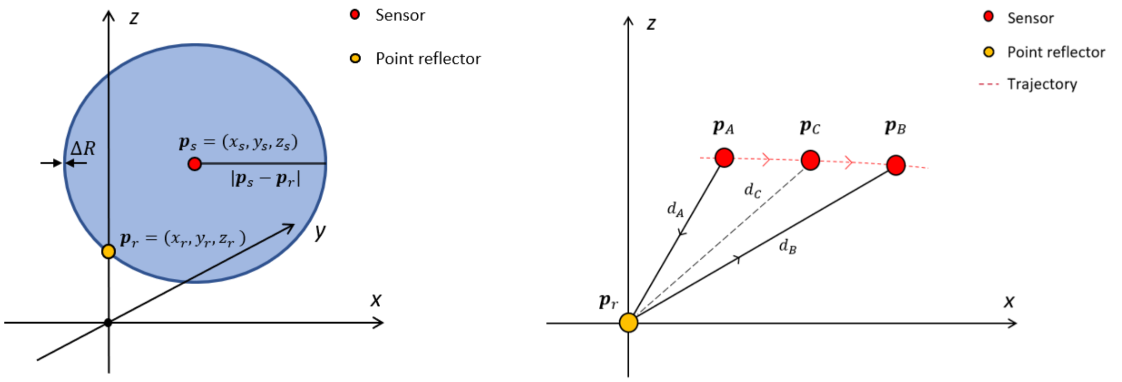

(a) Static sonar sensor and ideal point reflector

(b) Moving sonar sensor

Figure 3.2: Illustration of the time delay estimation problem. In (a) the delay for a static sonar sensor is simply given by the distance between the sensor and reflector. The blue sphere indicates all points with equivalent path length to that of the reflector. In (b), the sensor moves continuously, transmitting a short pulse at $\boldsymbol{p}_A$, and receiving the echo at $\boldsymbol{p}_B$. The phase centre is reached at $\boldsymbol{p}_C$, whose path length to $\boldsymbol{p}_r$ is used in the PCA to estimate the delay of the echo for the moving sensor.

A more advanced technique of estimating the delay is to solve for the delay using the sensor position. Consider Eq. 3.2, where t_{AC} is easily computed using Eq. 3.3. However, finding t_{CB} involves solving for time, because we have to find the time at which the moving sensor intersects the echo originating from $\boldsymbol{p}_r$ at $t = t_C$. The following method is proposed in this thesis to find t_{CB}:

$$t_{CB} = \underset{t}{\operatorname{argmin}} \big(||\boldsymbol{p}_s(t_C + t) - \boldsymbol{p}_r|| - ct \big)^2, \quad t \geq 0. \tag{3.5}$$

which finds the intersection of a sphere that extends linearly with time from p_r with the sensor position $\boldsymbol{p}_s(t)$, by minimising the squared error between the two. Thus, it is not necessary to assume any parameterization of the sensor trajectory, which can therefore be any arbitrary path. This method is expected to be more robust if the delay is large, as it takes in account the motion of the sensor when receiving the echo. An obvious disadvantage of this method is computational effort, as it involves an exhaustive search over a set of sensor positions. To limit the computational effort, only a small subset of sensor positions should be chosen and the delay estimation should not be performed on an unnecessarily fine grid. However, this method is not further used in this thesis, since the imaging scenarios considered are mostly short-range. In these scenarios the PCA provided adequate performance and is therefore preferred for its computational efficiency.

Spatially separated transmitter and receiver

Before we assumed that the transmit and receive sensor are co-located. However, it might be that the transmitter and receiver are spatially separated, which require an extension to the equations showed for estimating the delay. In this case, the delay of an echo can be written as the time it takes from transmitter to the reflector $t_{AC,T}$, plus the time it takes back to the receiver $t_{CB,R}$

$$\tau = t_{AC,T} + t_{CB,R} = \frac{1}{c}\big(||\boldsymbol{p}_{A,T} - \boldsymbol{p}_r|| + ||\boldsymbol{p}_r - \boldsymbol{p}_{B,R}||\big). \tag{3.6}$$

Applying the PCA approximation to estimate the path length from reflector back to the receiver, gives

$$\begin{aligned} ||\boldsymbol{p}_{A,R} - \boldsymbol{p}_r|| + ||\boldsymbol{p}_r - \boldsymbol{p}_{B,R}|| &\approx 2||\boldsymbol{p}_{C,R} - \boldsymbol{p}_r|| \\ \Longrightarrow ||\boldsymbol{p}_r - \boldsymbol{p}_{B,R}|| &\approx 2||\boldsymbol{p}_{C,R} - \boldsymbol{p}_r|| - ||\boldsymbol{p}_{A,R} - \boldsymbol{p}_r||, \end{aligned} \tag{3.7}$$

where $||\boldsymbol{p}_{A,T} - \boldsymbol{p}_r||$ is computed in the same way as Eq. 3.3, but for the transmitter position $\boldsymbol{p}_{s,T}$. The total delay is then approximated by

$$\tau_{PCA} = \frac{1}{c}\big(||\boldsymbol{p}_{A,T} - \boldsymbol{p}_r|| - ||\boldsymbol{p}_{A,R} - \boldsymbol{p}_r|| + 2||\boldsymbol{p}_{C,R} - \boldsymbol{p}_r||\big). \tag{3.8}$$

Alternatively, using the minimisation method given in Eq. 3.5, the delay can be solved by computing $t_{CB,R}$ as

$$t_{CB,R} = \underset{t}{\operatorname{argmin}}\big(||\boldsymbol{p}_s(t_{C,R} + t) - \boldsymbol{p}_r|| - ct\big)^2, \quad t \geq 0. \tag{3.9}$$

3.1.2 Signal model for point reflector

In this section, the signal model for a point reflector is given in terms of the delay found in the previous section. The model is then used to compute the signal response that would result from an ideal point reflector at some fixed position. Furthermore, we assume that the measured signal is a superposition of the individual contributions of the point reflectors in the image. Then, correlating the measured signal with the computed response of a point reflector at a given location, provides evidence for the presence of a point reflector at that location. This method is also known as a matched filter, and is computed for a set of discretized points in 3D (what is called a voxel, similar to a pixel in 2D) to make an image of the reflective structure. The signal delay τ is a continuous function of t, since the sensors are moving continuously while transmitting and receiving signal. However, the delay has to be computed on some discretized grid as the matched filter operates on discrete signals (samples). The resolution of the grid on which the delay is computed should be fine enough to maintain coherence, e.g., over a period of time short enough such that the sensors have moved only a small fraction of the wavelength.

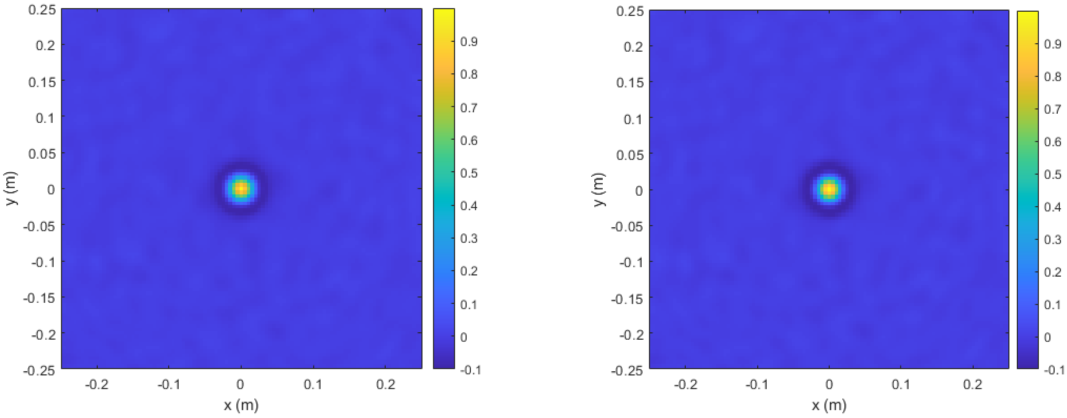

(a) PSF using bandpass signal (correlation)

(b) PSF using baseband signal (real part of complex correlation)

Figure 3.3: The PSF as resulting from a (normalised) matched filter per pixel, for a centred point reflector, as computed from the bandpass signal $s_T(t)$ in (a), and the baseband signal $s_{r,bb}(t)$ in (b).

The matched filter can be computed from the bandpass signal $s_r(t)$ or the directly from the baseband signal. Using the bandpass signal $s_r(t)$, the received signal is given by Eq. 2.23 as

$$s_r(t) = as_T(t - \tau(t)), \tag{3.10}$$

where τ(t) is the delay to the point reflector as a function over time. This model ignores that the attenuation of the signal a might vary over the duration of the measurement, as the sensor moves closer or further away from the point reflector. The discrete signal can be reconstructed by interpolating the transmit signal $s_T(t)$ with the estimated delays τ. The baseband expression for the received signal is given in Eq. 2.24 as

$$s_{r,bb}(t) = ag(t - \tau(t))e^{-j2\pi f_c \tau(t)}, \tag{3.11}$$

here the same function for delay is applied. Now the received signal of a point reflector in baseband (complex-valued) can be reconstructed by interpolating the baseband transmit signal $g(t)$ with $t - \tau(t)$, and applying a point-wise multiplication with the phase terms $e^{-j2\pi f_c \tau(t)}$.

To show equivalence of both methods, the resulting matched filter image is shown for a noise-free simulation of an ideal point reflector, also called a Point spread function (PSF). The delay was computing using the PCA, on a per-sample grid, and the signals are generated for a set of points in the xy-plane, using linear-interpolation. Shown in Figure 3.3, are the results of the simulation of one circular trajectory of the (co-located) transmitter and receiver at a radius of 0.5 meter, 1 meter above the point reflector. The transmit waveform is CW PRN with a bandwidth of 8 kHz, carrier of 8 kHz and a sampling rate of 48 kHz.

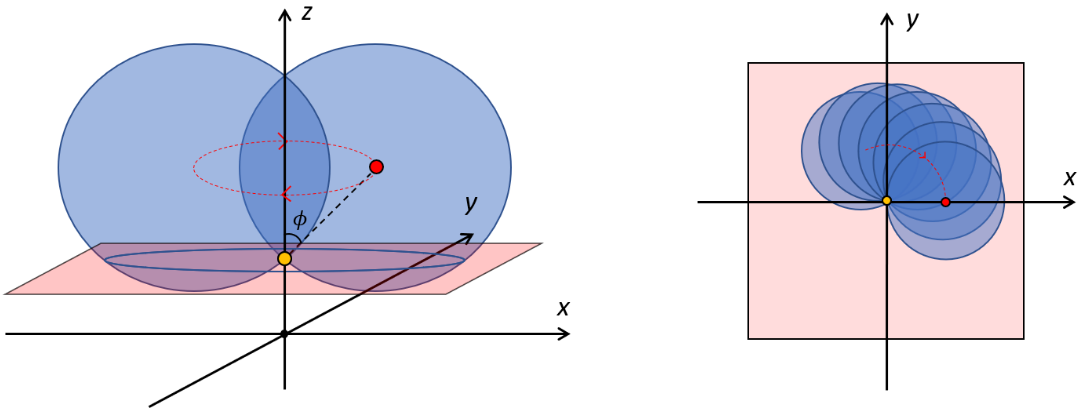

(a) Visualisation of the PSF in 3D

(b) PSF of partial trajectory in the xy-plane

Figure 3.4: Diagram of the imaging procedure. The co-located transmitter and receiver are on a circular trajectory at an angle ϕ to the point reflector as seen in (a). Here the PSF is imagined as a sum of short-time correlations while the sensor pair is moving over the trajectory, which provides a visual explanation of the PSF in 3D. Imaging in 2D, as seen for the xy-plane in (b), can then be understood by taking a slice of the 3D PSF.

3.1.3 Analysis of the PSF

The PSF essentially describes the correlation between the received signal from one point and that of other points in the image. The signal is transmitted and received continuously from a moving sensor, potentially spanning many pulses or a long CW signal. This can make it challenging to understand the signal's behaviour. Therefore, the PSF is imagined as a superposition of short-term correlations. Over a short period of time, the signal from a point reflector correlates with the transmit signal, which results in a spherical shell in the 3D image, centred at the position of the sensor at that time, as seen in Figure 3.2. Therefore, as the sensor moves over the trajectory, the signal of the point reflector will sum up coherently in the image at the actual location of the reflector, while the remaining surface of the spheres only partially overlap in space. This creates a mainlobe in the image at the location of the point reflector, and imaging sidelobes on the places where the spheres partially overlap. Intuitively, it can be understood that adjacent spheres sum up mostly on the outside of the shape that is traced out, and less on the inside of it. This effect can be seen in Figure 3.4 (b), where the outside of the circles mostly overlap on the edges of the traced figure.

The thickness of the spherical shells is given by the range resolution $\Delta R = \frac{c}{2B}$. It is important to note that the PSF is defined in 3D, as seen in Figure 3.4 (a). However, for a centred point reflector and a circular trajectory, the spherical shells have a constant radius and thus also a constant resolution component in the xy-plane. Therefore, the imaging resolution in the xy-plane can be obtained by using a tangent plane to approximate the surface of the spheres as they intersect the point reflector. The imaging resolution is then approximated by the xy-component of the tangent plane as

$$\Delta R_{xy} \approx \frac{1}{sin(\phi)} \Delta R, \tag{3.12}$$

where ϕ is the angle between the z-axis and the tangential component as seen in Figure 3.4. Therefore, the imaging resolution is only dependent on the range resolution of the waveform and the geometry of the trajectory with respect to the reflector. For example, for a trajectory with a large angle ($\phi \to 90$ deg), the resolution in xy is improved, but a poor resolution in z is obtained. Vice versa if the reflector is relatively deep with respect to the radius of the trajectory ($\phi \to 0$ deg), a good resolution in z but a poor resolution in xy is obtained.

When the position of the ideal point reflector is non-centred, the distances to the sensor will vary over its trajectory. This will create a more complicated PSF for non-centred points, which following the same logic, can be understood by the superposition of spheres (or circles in 2D) with varying radii. In Figure 3.5, the simulated PSFs for a circular trajectory are shown for four different points in the same xy-plane. The width of the mainlobe is consistent with $\Delta R_{xy} \approx 3$ cm for all four PSFs, thus Eq. 3.12 can be used for other points in the xy-plane as well. The centred PSF in Figure 3.5 confirms that the largest imaging sidelobes form a circle around the point reflector. In a similar fashion, more complicated sidelobe patterns are produced by imaging a non-centred point as seen in the remaining three figures. Notice that as the point reflector is placed further off-centre, or even outside of the circular trajectory of the sensor, the imaging sidelobes will start to overlap with the mainlobe of the point reflector. This means that if we image a scene inside of the circular trajectory, a strong reflector outside of the circle could produce sidelobes that overlap the image. This is obviously problematic, as a strong reflector could produce sidelobes that are stronger than the mainlobe of the reflectors in our scene, thereby potentially masking them.

Now that the effect of the position of the reflector with respect to the trajectory is understood, we consider the effect of the placement of the sensors in the xy-plane, in the case of a spatially separated transmitter and receiver. This could be required, for example, in the case of CW PRN as transmit signal. Similarly, as explained in chapter 2, the problem with using a CW signal is that direct path interference from the transmitter arises, resulting in sidelobes over the entire image. However, this section does not further discuss this particular problem as similar conditions can be applied as discussed in section 2.4. In Figure 3.6, the simulated PSF for a centred reflector is shown, where the transmitter and receiver rotate in the same direction, from various initial positions. The resulting imaging resolution is shown to be best when the receiver and transmitter are positioned close to each other. With the sensors at the same radius and 90-degree offset, the imaging resolution is worsened and area of coverage without imaging sidelobes is reduced. This effect is further exacerbated by placing one of the sensors in the centre. Finally, the imaging resolution in almost completely lost by placing the sensors opposite to each other.

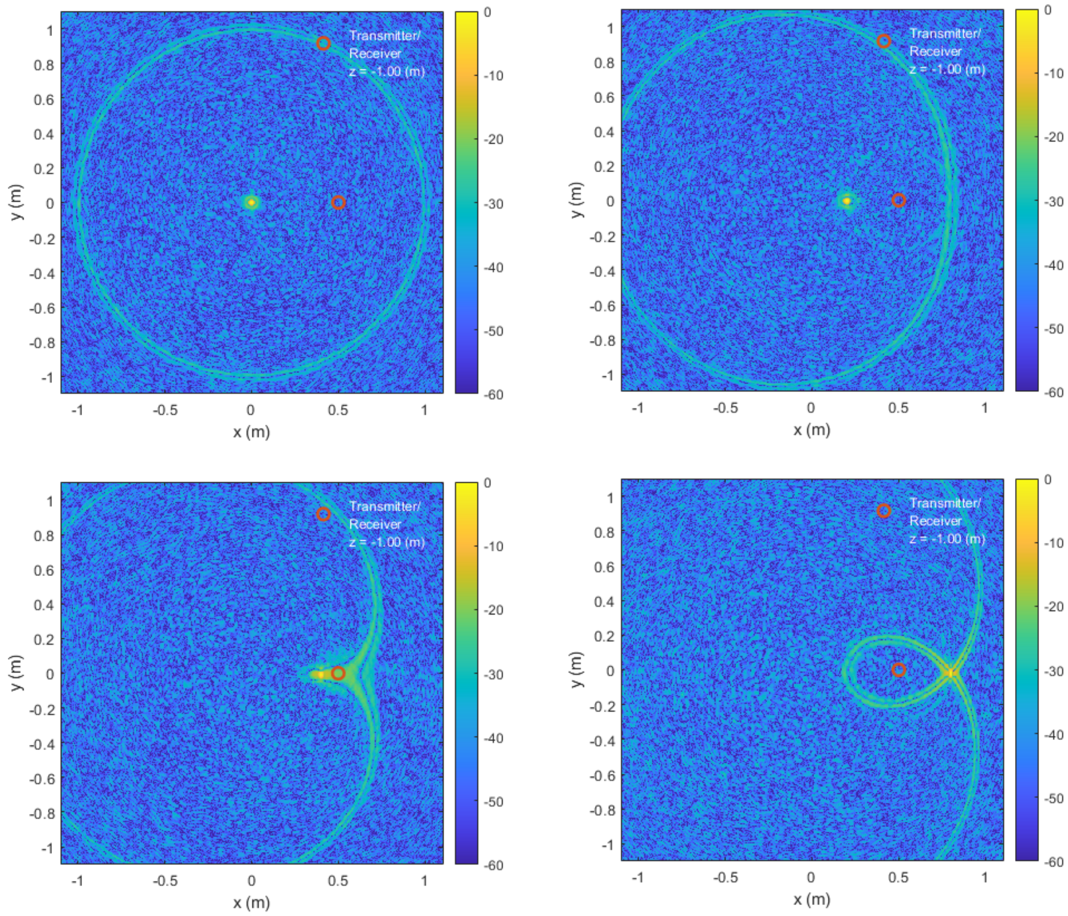

Figure 3.5: The imaging PSF (normalised in dB power) for four different points in the xy-plane ($z = -1.0$ m) using a circular trajectory and CW PRN as transmit waveform. The transmitter and receiver are co-located and make one full rotation in the xy-plane at $z = 0$ m. The starting position of the sensors $(x_0, y_0, z_0) = (0.5, 0, 0)$ is indicated by the red circle. The imaging sidelobes form a large circle around the point for point near the centre. The sidelobes start to bend inwards and create a loop, as the point moves outside of the circular sensor trajectory.

3.2 Inverse imaging

In this section, the aim is to enhance the imaging resolution and to suppress the imaging sidelobes that arise from the matched filter described in the previous section. Now that an intuitive understanding of the PSF has been established, the signal model in Eq. 3.11 is used to formalise the matched filter for imaging. Consider that the imaging domain is discretized in a number evenly-spaced voxels in x-y-z: $N = N_x N_y N_z$ and the underlying image is represented as a set of reflection coefficients: $\boldsymbol{v} = [v_1, v_2, \cdots v_N]^T$. Writing the received signal as a linear combination of the contributions from each voxel gives

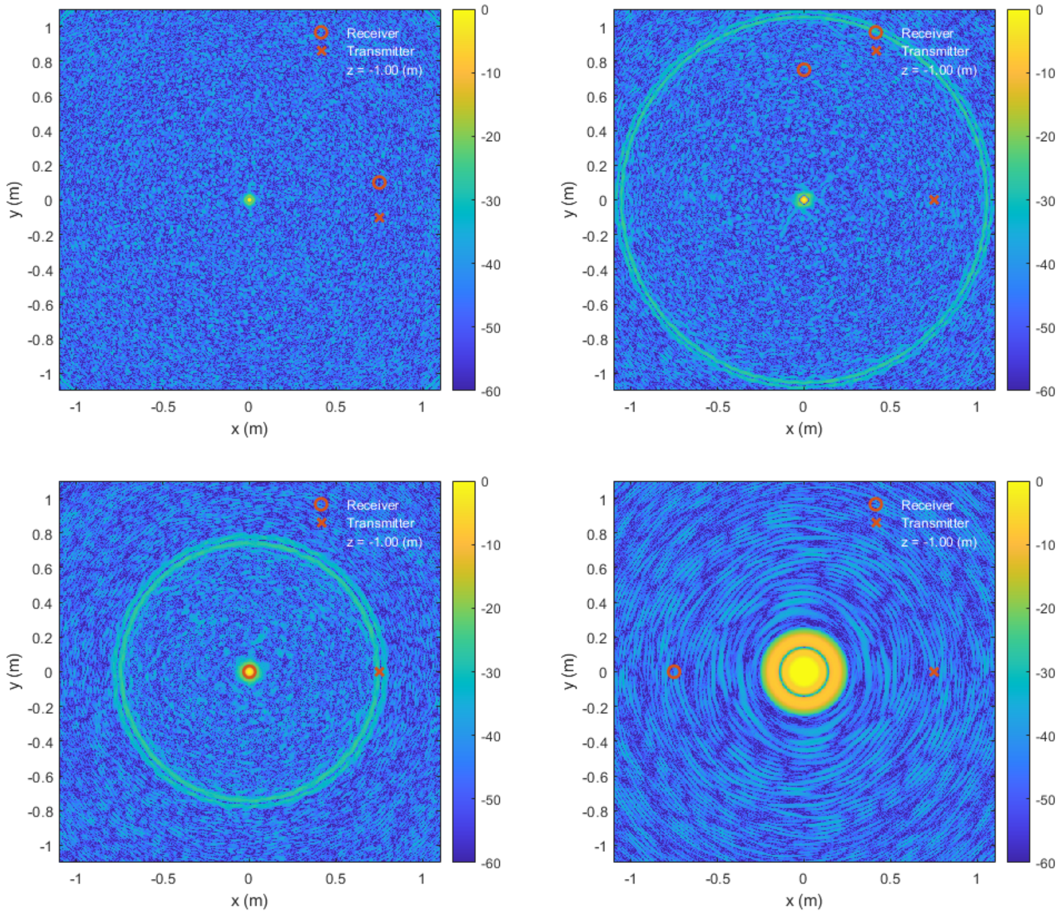

Figure 3.6: The imaging PSF (normalised in dB power) of a centred point reflector in the xy-plane ($z = -1.0$ m) for four separated transmitter and receiver configurations, ranking in imaging resolution from top-left to bottom-right. The receiver and transmitter follow a circular trajectory with a radius of the indicated starting point, given by the red circle and cross, respectively. The best resolution is achieved for a co-located sensor pair, and the worst when the sensors are opposing each other.

$$\boldsymbol{s}_{r,bb} = \boldsymbol{A}\boldsymbol{v}, \quad \boldsymbol{A} = \begin{bmatrix} | & | & & | \\ \boldsymbol{s}_{1,bb} & \boldsymbol{s}_{2,bb} & \dots & \boldsymbol{s}_{N,bb} \\ | & | & & | \end{bmatrix}. \tag{3.13}$$

Here the $N_{samples} \times N_v$ matrix $\boldsymbol{A}$ maps the set of point reflectors to the received baseband signal $\boldsymbol{s}_{r,bb}$. The correlation coefficient of the received signal and the signal of the n-th point reflector, is given by $\boldsymbol{s}_{n,bb}^H \boldsymbol{s}_{r,bb}$, where $\{.\}^H$ denotes the conjugate transpose. Ideally, the signal of a point reflector only correlates with the reference signal from the corresponding voxel. However, from the observed PSF in section 3.4 we know this is not the case, as partial correlations of the signals from different voxels create imaging sidelobes. Using Eq. 3.13, the matched filter for the complete image can be directly written as

$$\boldsymbol{v}_{MF} = \boldsymbol{A}^H \boldsymbol{s}_{r,bb}, \tag{3.14}$$

which is written in terms of the underlying image $\boldsymbol{v}$, using Eq. 3.13, as

$$\boldsymbol{v}_{MF} = \boldsymbol{A}^H \boldsymbol{A} \boldsymbol{v}. \tag{3.15}$$

Here $\boldsymbol{A}^H \boldsymbol{A}$ is an Hermitian matrix, whose entries are given by the inner products of the columns of matrix $\boldsymbol{A}$. Therefore, the model includes all the intervoxel correlations that arise from the matched filtering process. Thus, the PSF for each point in $\boldsymbol{v}$ is fully specified by $\boldsymbol{A}^H \boldsymbol{A}$.

3.2.1 Regularised least squares

By leveraging our knowledge of the imaging PSF, we can attempt to reverse its effect on the image. This is the idea of inverse imaging, where our goal is to reconstruct the underlying image $\boldsymbol{v}$ from the observed data, which is essentially an inverse problem. The difficulty with most inverse imaging problems is that they are inherently ill-posed [25], which means the solution is very sensitive to input disturbances such as noise or modelling errors. This poses a significant challenge in accurately recovering the underlying image from the observed data. To tackle these obstacles, this section will explore standard regularisation methods aimed at providing a feasible solution for the specific imaging problem at hand.

Consider the noise free signal model given in 3.13, where $\boldsymbol{A}$ might be a tall or wide matrix. The least squares solution for $\boldsymbol{v}$ is found by

$$\min_{\boldsymbol{v}} = ||\boldsymbol{A}\hat{\boldsymbol{v}} - \boldsymbol{s}||_2^2, \tag{3.16}$$

for which the closed form solution is given by

$$\hat{\boldsymbol{v}} = (\boldsymbol{A}^H \boldsymbol{A})^{-1} \boldsymbol{A}^H \boldsymbol{s}. \tag{3.17}$$

Here the matrix $(\boldsymbol{A}^H \boldsymbol{A})^{-1} \boldsymbol{A}^H = \boldsymbol{A}^\dagger$ is known as the pseudo-inverse of $\boldsymbol{A}$, where we directly estimate $\boldsymbol{v}$ from the observed data $\boldsymbol{s}$. This result can also be interpreted as the matched filter image $\boldsymbol{A}^H \boldsymbol{s}$, from which we estimate the underlying image by inverting for the PSF. This estimate can be computed if the inverse $(\boldsymbol{A}^H \boldsymbol{A})^{-1}$ exists, which is the case if the columns of $\boldsymbol{A}$ are linearly independent [26].

It might be that two columns are nearly identical, e.g. if they correspond to two neighbouring voxels. Therefore, the imaging grid itself is likely to have an influence on the conditioning of this inverse. The singular value decomposition (SVD) can be used to examine the conditioning of the matrix. The SVD of an $(m \times n)$ matrix is given by

$$\boldsymbol{A} = \underset{(m\times m)}{\boldsymbol{U}} \underset{(m\times n)}{\boldsymbol{\Sigma}} \underset{(n\times n)}{\boldsymbol{V}^H}, \tag{3.18}$$

where $\boldsymbol{U}$ and $\boldsymbol{V}$ are orthogonal matrices and $\boldsymbol{\Sigma}$ a diagonal matrix, containing the singular values of $\boldsymbol{A}$. The $(n \times n)$ matrix $\boldsymbol{A}^H \boldsymbol{A}$ can be written in terms of the SVD, as

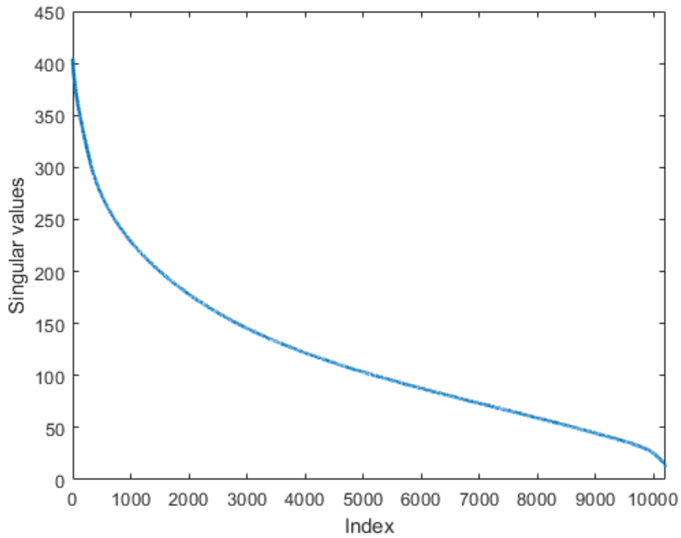

Figure 3.7: Singular values of matrix $\boldsymbol{A}$ in order of largest amplitude.

$$\boldsymbol{A}^H\boldsymbol{A} = (\boldsymbol{U}\boldsymbol{\Sigma}\boldsymbol{V}^H)^H(\boldsymbol{U}\boldsymbol{\Sigma}\boldsymbol{V}^H) = \boldsymbol{V}\boldsymbol{\Sigma}\underbrace{\boldsymbol{U}^H\boldsymbol{U}}_{\boldsymbol{I}}\boldsymbol{\Sigma}\boldsymbol{V}^H = \boldsymbol{V}\boldsymbol{\Sigma}^2\boldsymbol{V}^H. \tag{3.19}$$

The inverse of this matrix is determined from the SVD, as

$$\boldsymbol{V}\boldsymbol{\Sigma}^{-2}\boldsymbol{V}^H, \tag{3.20}$$

where the inverse of the singular values in $\boldsymbol{\Sigma}^2$ is given by

$$\boldsymbol{\Sigma}^{-2} = \begin{bmatrix} \frac{1}{\sigma_1^2} & & & \\ & \frac{1}{\sigma_2^2} & & \\ & & \ddots & \\ & & & \frac{1}{\sigma_n^2} \end{bmatrix}. \tag{3.21}$$

If one of the singular values goes towards zero, then this inverse becomes unstable. Therefore, a small constant is often added to the diagonal elements of the matrix. This process is known as regularisation and helps stabilise the inverse computation, by preventing division by small singular values. The regularised least squares estimate of $\boldsymbol{v}$ is given by

$$\hat{\boldsymbol{v}} = (\boldsymbol{A}^H\boldsymbol{A} + \lambda\boldsymbol{I})^{-1}\boldsymbol{A}^H\boldsymbol{s}, \tag{3.22}$$

where λ is the regularisation parameter. Notice that for $\lambda = 0$, the least squares solution given in Eq. 3.17 is obtained, and as $\lambda \to \infty$ the expression reduces to a scaled version of the matched filter: $\hat{\boldsymbol{v}}/\lambda \to \boldsymbol{A}^H\boldsymbol{s}$. Finding the optimal λ, which lies somewhere in between these two extremes, can be difficult.

In Figure 3.7 the singular values $\sigma_1, \sigma_2, \cdots \sigma_N$ are shown for for the imaging grid used to image the PSF in Figure 3.5. However, the imaging grid resolution is decreased to 2 cm ($\approx \lambda/2$) to be able to perform the SVD on a PC. What is noticed is that the matrix is full rank (no zero singular values), but there are many low singular values. It is not clear from the singular values, which contribute to the image and which could be discarded (e.g. by computing the inverse with a truncated SVD). Increasing the imaging resolution (smaller spacing between voxels), will lower the smallest singular values even further, thereby making the inverse computation less stable.

Direct methods for solving the least squares problem, such as in Eq. 3.22, require the matrix $\boldsymbol{A}$ to be stored in memory. However, for practical applications, the matrix quickly becomes too large to work with. For example, storing the $\boldsymbol{A}$ matrix for the 2D images seen in Figure 3.5 would already require over 100 GB of memory. Computing the matched filter image can luckily be performed in parallel, by computing the matrix vector products of $\boldsymbol{A}^H\boldsymbol{s}$. Then the matrix $\boldsymbol{A}^H\boldsymbol{A}$ could be computed separately, which could be smaller than storing $\boldsymbol{A}$ if the system contains more samples than voxels, but still contains $N_v \times N_v$ entries.

Alternatively, iterative methods designed for solving large linear systems exist, which only require to compute matrix vector products in each iteration, which can be done without storing the entire matrix in memory at once. In this thesis, LSQR is applied to iteratively solve the least squares problem, since it is considered numerically stable and only requires few iterations to converge [27]. The first iteration of LSQR uses the matched filter: $\boldsymbol{A}^H\boldsymbol{s}$ as an approximate solution, and subsequent iterations are used to refine the solution, which at each iteration provides a solution that is similar to regularised least squares [28].

3.3 Results

In this section the results for synthetic aperture imaging are given. First, a comparison of the PSF for the proposed waveforms plus noise is given in section 3.3.1. There, the methods of regularised least squares are applied to improve the PSF in terms of resolution and imaging sidelobes. Next, the results of the in-air demonstrator for imaging are provided in section 2.3.2.

3.3.1 Simulations

This chapter provided a few important simulation results in section 3.1.3, to explain the PSF resulting from a circular sensor trajectory. Supplementary, here the PSFs for PRN and HFM pulses are compared for both the matched filter and for regularised least squares, as seen in Figure 2.4. White Gaussian noise is added, to provide a more realistic least squares reconstruction, such that the received signal has an SNR of 10 dB in power. In total 5 seconds of HFM and PRN is integrated (with $PRI = T_p = 50$ ms, thus 100 pulses) to obtain the PSF images for a circular trajectory of the co-located sensor pair. The imaging resolution, as defined by the -8dB (in power) width of the mainlobe (see section 1.2.2), is approximately $\Delta R_{xy} \approx 2.5$ cm for PRN and $\Delta R_{xy} \approx 3.0$ cm for HFM. This is slightly higher than the mainlobe width of their autocorrelation: $\Delta R = \frac{c}{2B} \approx 2.1$ cm, as expected from the sensor trajectory. Interestingly, the matched

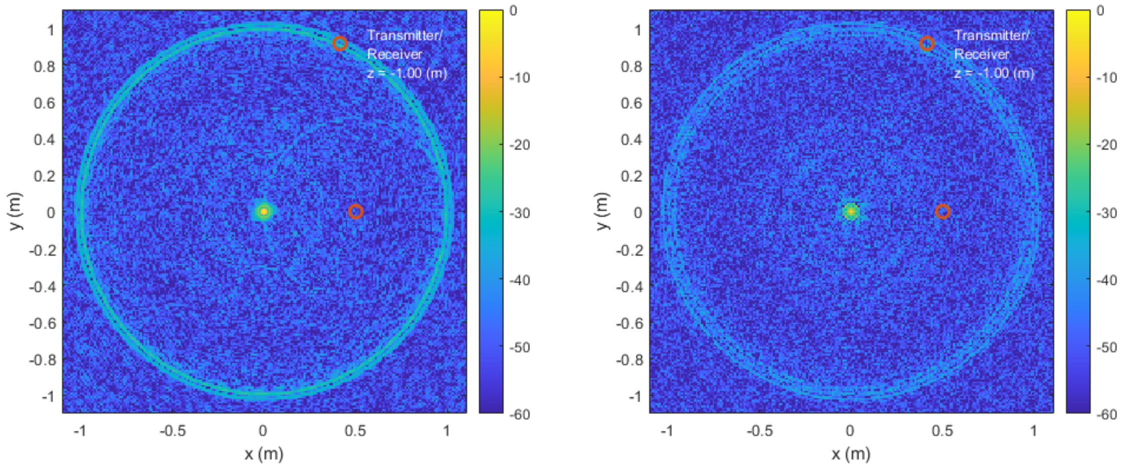

(a) Matched filter, PRN

(b) Regularised least squares, PRN

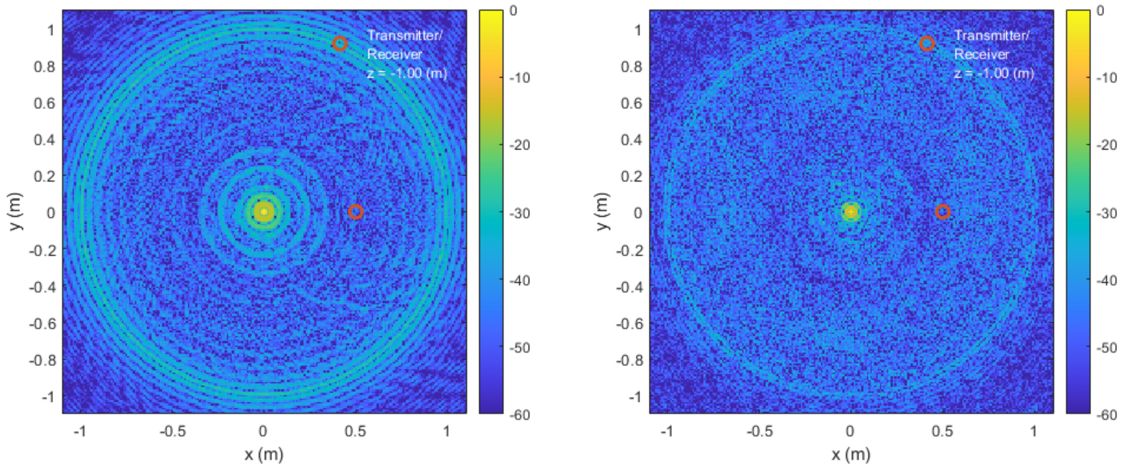

(c) Matched filter, HFM

(d) Regularised least squares, HFM

Figure 3.8: A comparison of the PSF for PRN and HFM pulses, as resulting from a matched filter and regularised least squares (implemented by 6 iterations of LSQR) on a 1 cm grid.

filter image for PRN shows lower sidelobe levels than for using HFM pulses, indicating that PRN results in less inter-pixel correlation than HFM.

In Figure 3.8 (b) and (d) the PSF resulting from a least squares estimate is given, which is implemented using LSQR. The algorithm is stopped after 6 iterations, after which the residual error did not significantly decrease any further. The resulting imaging resolution improved to approximately $\Delta R_{xy} \approx 2$ cm for both waveforms. The imaging sidelobes for PRN, formed by the circle with a radius of 1 meter, were at a level of about -30 dB in the matched filter, and are suppressed to about -40 dB using the least squares algorithm. Similarly, a suppression of about 10 dB was achieved with least squares for HFM, but the PSF exhibits a higher peak to sidelobe than for PRN.

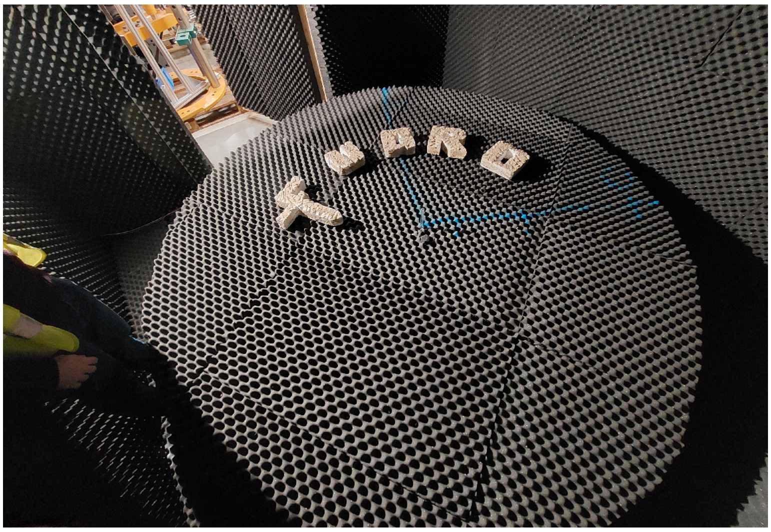

Figure 3.9: Picture of the rotating table, taken inside the in-air demonstrator. Seen is the 'Fugro' logo made from sanded styrofoam letters.

3.3.2 In-air measurements

In this sections the results of the in-air measurements for synthetic aperture imaging are provided. The goal of these measurements is to see how the methods provided in this section perform on real data, including the effect of any unwanted interference such as noise. The schematic of this setup was provided in the start of this chapter in Figure 3.1. Furthermore, a picture taken inside the anechoic room is given in Figure 3.9, where the imaging scene is seen. The scene consists of a set of styrofoam letters with some surface roughness and a layer of sand for increased acoustic contrast. The images in this section are given using a linear scale, instead of decibels, since using positive and negative correlation values provided the most informative representation of the image.

The in-air demonstrator for imaging suffers from the interference of static reflections in the room (clutter), similarly as in the moving target measurements provided in section 2.3.2. This is a disadvantage of the measurement setup, since the relative motion between the scene and sensors is achieved by rotating the scene, while keeping the sensors fixed. In practice this would be reversed, i.e., static scene and a moving sensor pair (e.g. from a moving ship), in which the reflections from the environment are not static. Since the interfering static reflections are essentially the same as during the moving target measurements, the filtering methods proposed in section 2.2.3 are also applied for these measurements. The distance of the imaging grid to the sensors (thus delay) is estimated from the angle of the rotating table, which is measured using a 12 bit encoder (encoding the angle in 4096 discrete steps) over one full rotation. The audio interface seen in Figure 2.12 provides synchronous recording of the microphone signals, the analog transmit signal fed to the loudspeaker and the encoder signal at a sampling rate of 48 kHz. Using these three signals, the matched filter image can be constructed, using the methods explained in section 3.1.

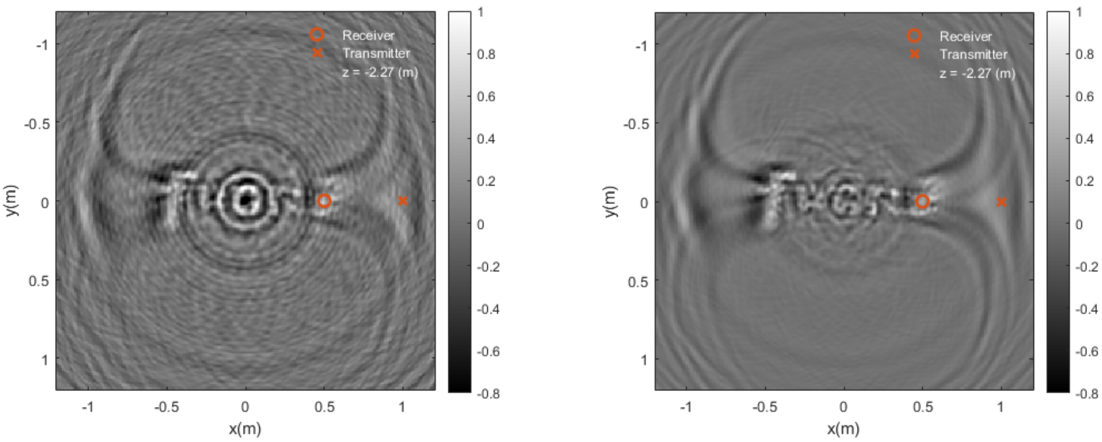

(a) Matched filter image

(b) Matched filter image after clutter filter

Figure 3.10: Matched filter image for a centred logo. Static reflections are seen to create concentric rings in the image (a), which are removed in (b) using the CLEAN procedure. Furthermore, imaging sidelobes are created for the letters that partly come under the sensor pair, as expected from the PSF.

Initially, the logo is placed in the middle of the table with a microphone (receiver) at $\boldsymbol{p}_r = (0.5, 0, 0)$ m and loudspeaker (transmitter) at $\boldsymbol{p}_t = (1, 0, 0)$ m. A matched filter image for the centred logo using CW PRN as transmit signal is provided in Figure 3.10. The imaging grid is defined by a xy-plane at $z = -2.27$ m, where $z = 0$ m is the plane containing the sensors. Noticed from Figure 3.10 (a) is that the static reflections create concentric circles in the image. Static reflections experience no Doppler shifts, therefore the corresponding signals are expected to correlate somewhere in the centre of the circular trajectory (along z-axis), since for these points the delay remains constant over the sensor trajectory. However, if that point is not in the same height (z) as the image, then only its imaging sidelobes will be observed. Therefore, the concentric imaging artefacts can be interpreted as imaging sidelobes of the static reflections. In Figure 3.10 (b) the clutter interference is filtered out using the CLEAN procedure (1000 iterations), which largely removes the imaging artefacts. In Figure 3.10, the outer letters ('F' and 'O') show significant imaging sidelobes, as expected from the PSF for a point that comes under the sensor trajectory. Therefore, the images are expected to improve in terms of resolution and imaging sidelobes by placing the sensor further out from the centre.

Next, the logo is placed away from the centre as seen in Figure 3.9 to avoid overlap of the logo with the imaging artefacts. Additionally, the bulb used for the moving target experiments is placed below the logo to see the imaging sidelobes of a point-like reflector. In Figure 3.11 (a) the matched filter image is given for a receiver at $\boldsymbol{p}_{m_1} = (0.5, 0, 0)$ m. This produces a low resolution image of the scene, since the placement of the logo with respect to the receiver is non-ideal. To see if (regularised) least squares can help improve the resolution in this case, 6 iterations

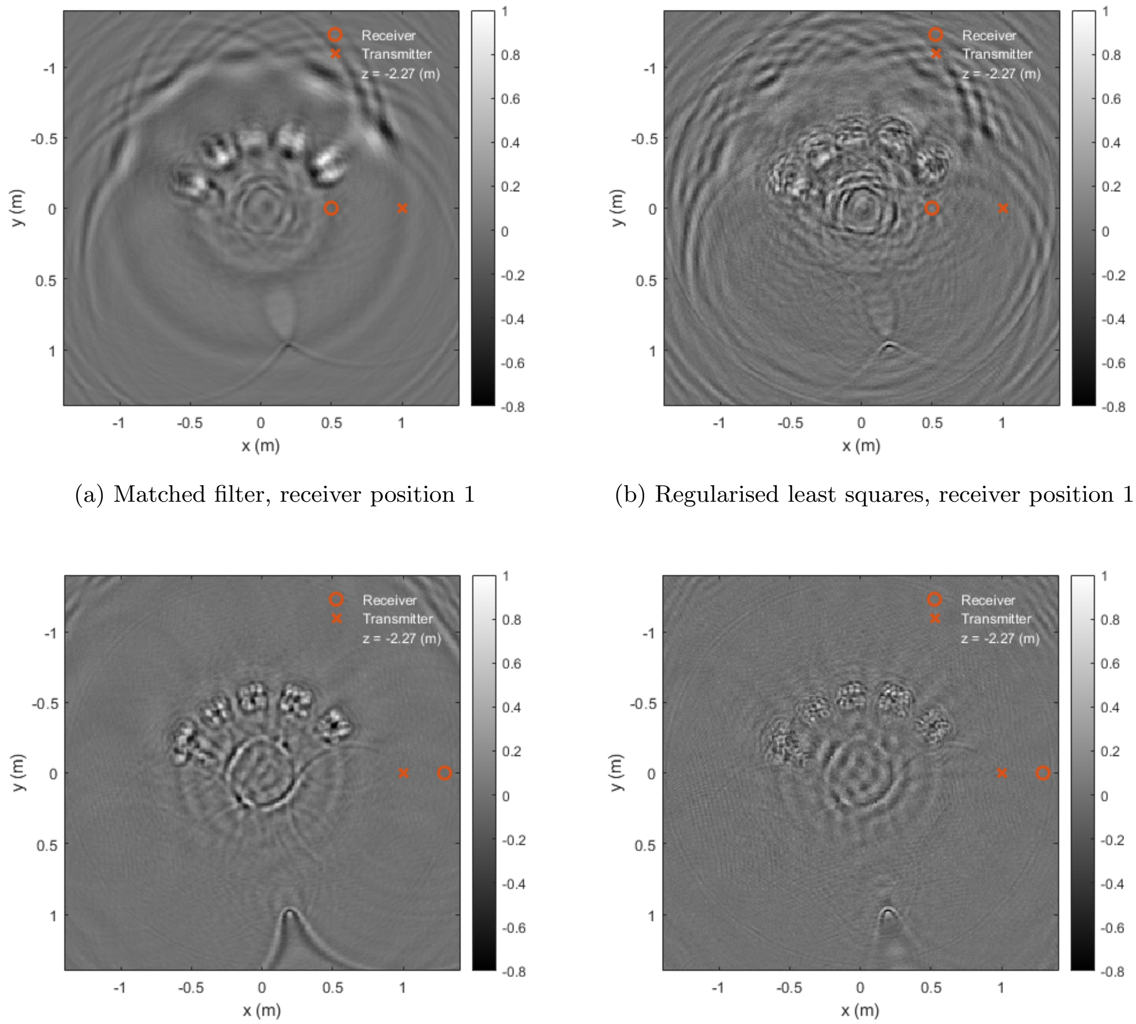

(a) Matched filter, receiver position 1

(b) Regularised least squares, receiver position 1

(c) Matched filter, receiver position 2

(d) Regularised least squares, receiver position 2

Figure 3.11: Matched filter and regularised least squares images using CW PRN + CLEAN for a microphone positioned at $\boldsymbol{p}_{\boldsymbol{r_1}} = (0.5, 0, 0)$ m in (a) and (b) and $\boldsymbol{p}_{\boldsymbol{r_2}} = (1.3, 0, 0)$ m in (c) and (d). The resolution achieved with position 1 is poor, as expected from the placement of the logo nearly under the sensor pair, but improves by placing the sensor further from the centre as seen in (c). Regularised least squares, implemented with 6 iterations of LSQR, is applied in attempt to improve the imaging resolution. The resolution appears to improve using RLS, but the logo is better visible using a matched filter.

of LSQR are applied as shown in Figure 3.11 (b). In Figure 3.11 (c), the matched filter image is given for a receiver at $\boldsymbol{p}_{m_1} = (1.3, 0, 0)$ m and similarly, 6 iterations of LSQR are applied to this measurement. The resulting image is seen in 3.11 (d), from which it is concluded that the imaging resolution appears to increase using the least squares method. However, placing the sensors further out, such that the imaging PSF improves, seems to have more effect on the overall image quality than least squares.

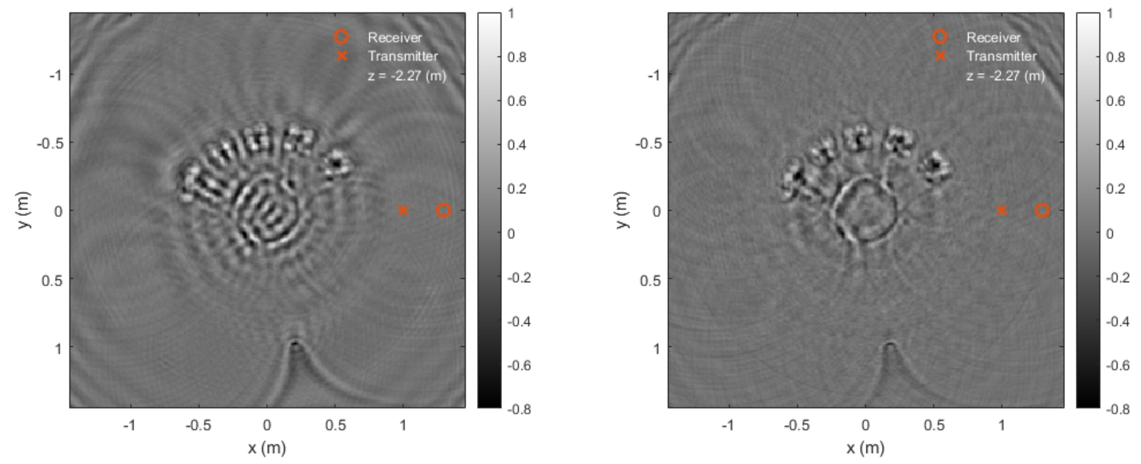

(a) HFM (b) PRN

Figure 3.12: Matched filter images using HFM (a) and PRN pulses (b). Clutter interference is filtered out using CLEAN for both HFM and PRN. The observed sidelobe levels for HFM are higher than for PRN.

Finally, HFM and PRN pulses are compared using the same imaging scene. Similarly to the pulsed measurements for moving target detection (section 2.3), a $PRI = 50$ ms and a pulse duration $T_p = 5$ ms is used at $f_c = 8$ kHz with $B = 8$ kHz. Now CLEAN is applied to both HFM and PRN pulses, since it is not straightforward how to apply the MTI filter to imaging without corrupting the image. Figure 3.12 shows the resulting matched filter images. While the image using HFM pulses appears to have slightly more contrast on the letters, PRN pulses appear to image the scene with a higher resolution and lower sidelobe levels.

3.4 Discussion and Conclusion

In this chapter, the concept of coherent integration is explored for high-resolution imaging using a single acoustic sensor. The key assumption is that the position of the sensor is known accurately over time, such that coherence can be maintained over a long sensor trajectory. In part, this is facilitated by the use of relatively low frequencies (thus long wavelengths), which requires less positioning accuracy.

The first question posed in the start of this chapter: "*How to process the received echoes in order to achieve coherent integration from a moving sensor pair?*", is answered in section 3.1.1, where the methods for estimating the propagation delay are discussed. It is assumed that the echo has a constant attenuation factor over the sensor trajectory. However with a varying distance the attenuation might change, e.g., due to spherical spreading, which might have played a role in the imaging result from the in-air demonstrator. In this thesis, the phase centre approximation (PCA) is used to in simulations and processing of the measured data. Additionally, an alternative (more advanced) method is proposed, which takes in account the motion of the receiving sensor. However, this method is not further investigated in this thesis and is therefore also considered as future work.

To be able to answer the second question: "*What are the key parameters that influence the imaging resolution, and how can it be improved?*", it is important to understand how the point spread function (PSF) is established, which is explained in detail in section 3.1.3. There, an intuitive explanation of the PSF is provided, and more complex scenarios, such as a non-centred point, or spatially separated receive and transmit sensors, are analysed with simulations of the PSF. What is observed from the PSF is that a point outside of the (circular) trajectory of the sensors can create imaging sidelobes that overlap with the image of the scene. Therefore, methods to suppress the echoes from outside the imaging scene, should be investigated further. The range resolution and imaging sidelobes are seen to be dependent on the geometry of the sensor trajectory with respect the imaged point. In the xy-plane, increasing the radius of the circular trajectory is seen to improve the imaging resolution. Furthermore, the optimal sensor placement in terms of resolution and sidelobes is expected to be achieved using a co-locating the sensors. In section 3.2, the PSF is treated as a linear system of equations, and an extension to improve upon the matched filter image is explored through the use of regularised least squares. The results of least squares are given in section 3.3, where the PSF is seen to improve upon the matched filter in terms of mainlobe resolution and suppression of the imaging sidelobes.

The comparison of HFM and PRN is repeated for the PSF, which revealed that PRN has the least inter-voxel correlation, leading to lower sidelobe levels compared to HFM. Interestingly, this conclusion is the exact opposite of what we have found for moving target target detection, where HFM excelled in terms of sidelobe performance.

Finally, the methods are verified on real data in section 3.3.2, in which a (more complex) scene is imaged in 2D. The observations mostly agree with the simulation results, in that the resolution is improved by the proper sensor placement and that HFM produces more imaging sidelobes than PRN. An application of least squares to real data is seen, which appears to improve the imaging resolution and sidelobe levels, but decreased the image contrast. Furthermore, modelling errors were introduced by the static reflections in the measurement setup, which was partly solved with a clutter filter, but is thought to have limited the effectiveness of least squares.

4 Conclusion

In this thesis, coherent integration is used to improve the imaging and detection capabilities of an active sonar under low SNR conditions. For these two applications, high duty-cycle transmit pulses are considered for maximising the signal energy, comparing chirps (HFM) with pseudo-random noise (PRN). Furthermore, coherent integration over multiple pules is explored to maximise the post-processing SNR. This is shown to overcome some of limitations of sonar systems for imaging and detection, which typically rely on a minimum signal strength of a single echo.

In chapter 2, a processing method is proposed for moving target detection, which uses a signal model for constant velocity targets. Coherent integration is achieved in a computationally efficient manner, by integrating over short-time correlations of the echo and transmit signal using the Radon-Fourier transform (RFT). The interference of clutter signals is tackled using clutter filtering: CLEAN + MTI for PRN and an MTI filter for HFM. The methods are tested on synthetic data and on real data measured in the in-air demonstrator, from which it is concluded that the post-processing SNR is improved compared to processing a single echo. It is demonstrated that HFM pulses, which are maximally ambiguous in range-Doppler, can unambiguously resolve a moving target through integration over multiple pulses. It is shown that the resulting peak to sidelobe ratio is superior to that of PRN pulses. Furthermore, the clutter interference is suppressed more effectively using HFM, allowing for better target detection in clutter-dominated environments.

In chapter 3, the processing methods for synthetic aperture imaging are discussed. The main assumption is that the sensor position is accurately known over time, which is used to model the received signal using delay estimation techniques. Subsequently, a matched filter for imaging is proposed, and the resulting point-spread function (PSF) is analysed for a circular sensor trajectory. This has provided valuable insight on how to obtain the best imaging resolution in terms of the sensor placement. Most importantly, the imaging resolution is improved by placing the sensors closer to each other and at an increased radius. Furthermore, it is demonstrated that the imaging performance of PRN is superior to HFM, as it achieves lower sidelobe levels. Additionally, a least squares algorithm is applied, which is shown to improve the imaging resolution and effectively suppress imaging sidelobes. The methods for imaging are tested in the in-air demonstrator, which verified the proposed methods. However, modelling errors, due to the interference of reflectors outside of the image are thought to have limited the effectiveness of least squares.

4.1 Future work

An interesting consideration for future work is to investigate if the proposed (RFT-based) method for moving target detection can be generalised, so that it can applied to synthetic aperture imaging. The image would then be obtained by a per-voxel integration over the range-time image, which contains the pulse compressed echoes. In contrast to moving target detection, the integral will not be over a straight line, but over a curve, which makes it more difficult to find the Doppler component on that line. However, successful implementation of this technique might give a more computationally efficient method for imaging. Furthermore, it expected to facilitate other clutter filtering techniques than CLEAN, such as MTI, which would improve the clutter suppression that can be achieved.

Another crucial area for future work is the extension of the presented processing methods for a single sonar sensor to an array of sensors. This will improve the imaging and detection capabilities by providing directional signal transmission and reception, using beamforming techniques. This could have several advantages for moving target detection, including improved target localisation, increased SNR, and the ability to focus the transmit pulse in the plane of the (shallow) water. This could provide similar advantages to synthetic aperture imaging, for example by steering the transmit pulse towards the region of interest, or to suppress signals received from outside of the region of interest, which could help mitigate imaging sidelobes.

A practical disadvantage of lowering the frequency is that it necessitates a larger spacing between the sensors elements, which means that fewer sensors can be packed in the same space. Therefore, it is crucial to consider the array implementation in order to conclude whether or not the proposed methods can actually improve imaging and detection performance compared to high frequency systems that rely on beamforming of a single pulse echo.

Taking a wider view, it is important to realise that the methods in this thesis rely on a number of assumptions that might not hold in a real-world application. If left unnoticed, these factors could introduce modelling errors and should therefore be considered carefully. For example, it is assumed that the medium has a constant propagation speed, which in water might vary due to differences in temperature or salinity. Additionally, there might be dynamic changes in the environment, such as the motion of the sea surface, which are currently not taken into account in the proposed methods. These factors could significantly impact the performance of the proposed clutter filtering techniques in a marine environment.

Bibliography

[1] Georg Wiora. *Principle of active sonar*. 2005. URL: https://commons.wikimedia.org/wiki/File:Sonar_Principle_EN.svg (visited on 06/09/2023).

[2] Ronald Kessel and Reginald Hollett. "Underwater Intruder detection sonar for harbour protection: state of the art review and implications". In: (Nov. 2006).

[3] B.D. Van Veen and K.M. Buckley. "Beamforming: a versatile approach to spatial filtering". In: *IEEE ASSP Magazine* 5.2 (1988), pp. 4–24. DOI: 10.1109/53.665.

[4] Roy Edgar Hansen. "Introduction to Synthetic Aperture Sonar". In: *Sonar Systems*. Ed. by N. Z. Kolev. Rijeka: IntechOpen, 2011. Chap. 1. DOI: 10.5772/23122. URL: https://doi.org/10.5772/23122.

[5] Roy Hansen. "Synthetic Aperture Sonar Technology Review". In: *Marine Technology Society Journal* 47 (Sept. 2013), pp. 117–127. DOI: 10.4031/MTSJ.47.5.5.

[6] Marc Pinto. *Design of synthetic aperture sonar systems for high-resolution seabed imaging*. Tutorial, OCEANS'06 MTS/IEEE Boston, Massachussets, USA, 18-21 September 2006.

[7] Michael P. Hayes and Peter T. Gough. "Synthetic Aperture Sonar: A Review of Current Status". In: *IEEE Journal of Oceanic Engineering* 34.3 (2009), pp. 207–224. DOI: 10.1109/JOE.2009.2020853.

[8] A. Douglas. *Underwater Acoustic Signal Processing*. Mar. 2019, pp. 33–93.

[9] Mathieu Colin, Peter Beerens, and Michael Ainslie. "Optimum sonar frequency for diver detection in harbors". In: vol. 29. Jan. 2007.

[10] Bassem R. Mahafza. *Radar Systems Analysis and Design Using MATLAB*. USA: CRC Press, Inc., 2000. ISBN: 158488228X.

[11] Mark A. Richards et al. *Principles of modern radar*. Vol. 1. Scitech Publishing, 2010. Chap. 8.2.

[12] Daniel Sjöberg. *Radar and Remote Sensing Lecture 11: Fundamentals of pulse compression waveforms*. EITN90 Radar and Remote Sensing, Lecture 11, Spring 2020. Lund University.

[13] Mark A. Richards et al. *Principles of modern radar*. Vol. 1. Scitech Publishing, 2010. Chap. 20.3.

[14] Dennis Ward Ricker. *Echo Signal Processing*. USA: Kluwer Academic Publishers, 2003. Chap. 4. ISBN: 140207395X.

[15] D.A. Swick. *An ambiguity function independent of assumptions about bandwidth and carrier frequency*. 1966.

[16] J. Yang and Tapan Sarkar. "Doppler invariant property of hyperbolic frequency modulated waveforms". In: *Microwave and Optical Technology Letters* 48 (June 2006), pp. 1174–1179. DOI: 10.1002/mop.21573.

[17] Yves Doisy et al. "Target Doppler estimation using wideband frequency modulated signals". In: *IEEE Trans. Signal Process.* 48.5 (2000), pp. 1213–1224. DOI: 10.1109/78.839970.

[18] Mathieu Colin and Peter Beerens. "False-Alarm Reduction for Low-Frequency Active Sonar With BPSK Pulses: Experimental Results". In: *Oceanic Engineering, IEEE Journal of* 36 (Feb. 2011), pp. 52–59. DOI: 10.1109/JOE.2010.2094770.

[19] G. Jourdain and J. P. Henrioux. “Use of large bandwidth duration binary phase shift keying signals in target delay Doppler measurements”. In: *The Journal of the Acoustical Society of America* 90.1 (1991), pp. 299–309. DOI: 10.1121/1.401300.
[20] Nikita Petrov. “Migrating Target Detection in Wideband Radars”. PhD thesis. Delft University of Technology, 2019. DOI: 10.4233/uuid:08556a7c-ef90-43f7-998b-f103ceea6267.
[21] Francois Le Chevalier. *Principles of radar and sonar signal processing*. Jan. 2002.
[22] Mark A. Richards et al. *Principles of modern radar*. Vol. 1. Scitech Publishing, 2010. Chap. 17.4.
[23] Krzysztof Kulpa. “The CLEAN type algorithms for radar signal processing”. In: *2008 Microwaves, Radar and Remote Sensing Symposium*. 2008, pp. 152–157. DOI: 10.1109/MRRS.2008.4669567.
[24] Jia Xu et al. “Radon-Fourier Transform for Radar Target Detection, I: Generalized Doppler Filter Bank”. In: *IEEE Transactions on Aerospace and Electronic Systems* 47.2 (2011), pp. 1186–1202. DOI: 10.1109/TAES.2011.5751251.
[25] Per Christian Hansen. *Rank-deficient and discrete ill-posed problems*. SIAM Monographs on Mathematical Modeling and Computation. Numerical aspects of linear inversion. Philadelphia, PA: Society for Industrial and Applied Mathematics (SIAM), 1998. ISBN: 0-89871-403-6.
[26] S. Boyd and L. Vandenberghe. *Introduction to Applied Linear Algebra*. Cambridge University Press, 2008. Chap. 10.1.
[27] Christopher C. Paige and Michael A. Saunders. “LSQR: An Algorithm for Sparse Linear Equations and Sparse Least Squares”. In: *ACM Trans. Math. Softw.* 8.1 (Mar. 1982), pp. 43–71. ISSN: 0098-3500. DOI: 10.1145/355984.355989. URL: https://doi-org.tudelft.idm.oclc.org/10.1145/355984.355989.
[28] Per Christian Hansen. *Discrete Inverse Problems*. Society for Industrial and Applied Mathematics, 2010. DOI: 10.1137/1.9780898718836. URL: https://epubs.siam.org/doi/abs/10.1137/1.9780898718836.

Appendix A

The ambiguity function as an inverse Fourier transform

Consider the narrowband ambiguity function $\chi_{\text{NB}}(\tau, f_D) = \int_{-\infty}^{\infty} s(t)s^*(t-\tau)e^{j2\pi f_D t}dt$, with a substitution $t' = t - \tau$:

$$\chi_{\text{NB}}(\tau, f_D) = \int s^*(t')s(t'+\tau)e^{j2\pi f_D (t'+\tau)}dt'. \tag{A.1}$$

In this form, the ambiguity function for a fixed f_D can be written as a convolution:

$$\chi_{\text{NB}}(\tau, f_D) = s^*(-t') * \big(s(t')e^{j2\pi f_D t'}\big). \tag{A.2}$$

Using the convolution theorem, $\chi_{\text{NB}}(\tau, f_D)$ is given by the inverse Fourier transform as

$$\chi_{\text{NB}}(\tau, f_D) = \mathcal{F}^{-1}\Big(\mathcal{F}\big(s^*(-t')\big) \cdot \mathcal{F}\big(s(t')e^{j2\pi f_D \tau}\big)\Big), \tag{A.3}$$

whose components are given by

$$\mathcal{F}\big(s^*(-t')\big) = S^*(f), \tag{A.4}$$

$$\mathcal{F}\big(s(t')e^{j2\pi f_D t'}\big) = \int s(t')e^{j2\pi f_D t'}e^{-j2\pi f t'}dt' = \int s(t')e^{-j2\pi (f-f_D)t'}dt' = S(f - f_D). \tag{A.5}$$

Therefore, the ambiguity function can be written as an inverse Fourier transform:

$$\chi_{\text{NB}}(\tau, f_D) = \int S^*(f)S(f - f_D)e^{j2\pi f \tau}df. \tag{A.6}$$

This is used to show that the last step in Eq. 2.43 can be written using the narrowband ambiguity function of the baseband signal $g(t)$:

$$\int G(f - f_c\frac{2v}{c})G^*(f)e^{j2\pi f t''}df = \chi_{g,\text{NB}}\big(t'', f_c\frac{2v}{c}\big), \tag{A.7}$$

if we substitute $s(t) = g(t)$, $\tau = t''$ and $f_D = f_c\frac{2v}{c}$ in Eq. A.6.